

Modified Teukolsky formalism: Null testing and numerical benchmarking

Fawzi Aly^{1,*}, Mahmoud A. Mansour^{2,†}, Luis Lehner^{3,‡}, Dejan Stojkovic^{1,§}, Dongjun Li^{4,¶} and Pratik Wagle^{5,**}

¹*HEPCOS, Physics Department, SUNY at Buffalo, Buffalo, New York, USA,*

²*Physics Department, The University of Tokyo, Kashiwanoha, Kashiwa, Chiba 277-8574, Japan,*

³*Perimeter Institute for Theoretical Physics, 31 Caroline St., Waterloo, ON, N2L 2Y5, Canada,*

⁴*Illinois Center for Advanced Studies of the Universe & Department of Physics and*

⁵*Max Planck Institute for Gravitational Physics (Albert Einstein Institute), D-14476 Potsdam, Germany*

(Dated: March 11, 2026)

Next-generation gravitational-wave detectors will make black-hole ringdown an increasingly sensitive probe of small departures from General Relativity in the strong-field regime. This motivates obtaining high-precision predictions of gravitational effective field theory, as spectral shifts can be quite small. Here we perform a focused stress test of the modified-Teukolsky framework by designing two null diagnostics. First, we consider an action with redundant operators that must produce zero first-order vacuum QNM shifts. Second, we exploit a Ricci-flat identity relating two physical cubic Riemann theories to test such a relation is satisfied by the ringdown spectra obtained. We compute the shifts using two independent numerical approaches: the eigenvalue-perturbation and generalized continued-fraction (Leaver-type) methods. Both null tests are passed across multiple multipoles and overtones, and the control-operator results agree in magnitude with the benchmark values reported in Ref. [1]. These validations support using the framework for obtaining accurate predictions for robust strong-field tests, with straightforward extensions to rotating backgrounds and coupling with matter fields.

I. INTRODUCTION

With next-generation ground- and space-based detectors—Einstein Telescope, Cosmic Explorer, and LISA—on the horizon, sensitivity and bandwidth will expand substantially, enabling more precise probes of the nonlinear, dynamical regime in which any departures from General Relativity (GR), if present, may manifest [2–6]. This motivates effective-field-theory (EFT) extensions of gravity—one branch within the broader landscape of beyond-GR models—which encode high-scale physics through controlled higher-derivative and non-minimal couplings that remain consistent with weak-field bounds yet can yield clean strong-gravity signatures [1, 7].

Black-hole ringdown is a standard testbed for beyond-GR imprints: EFT induced deformations can shift GR quasinormal-mode (QNM) spectra, break even/odd isospectrality, and introduce additional radiative degrees of freedom that alter excitation and damping [8–12]. These expectations can be modeled via perturbatively equivalent strategies: (i) derive and solve *modified master equations* with deformed potentials (modified Teukolsky/Regge–Wheeler–Zerilli (RWZ)) [1, 7]; or (ii) work perturbatively in the EFT couplings so the GR Teukolsky/RWZ operator acts on the corrections, sourced by the GR gravitational perturbation (up to first order in book-keeping parameter ϵ) and any effec-

tive matter source [10, 13, 14]. Moreover, QNM shifts could be computed via various techniques for instance (a) the *eigenvalue perturbation* (EVP) method [10, 15, 16], (b) *direct integration* with asymptotic matching [17] and (c) *generalized continued-fraction* (Leaver-type) schemes adapted to the modified equations [7, 18, 19].

Demonstrations span both parity-preserving and parity-violating sectors: in higher-derivative gravity (HDG), high-order slow-rotation expansions reproduce Kerr QNM shifts with good accuracy up to $a/M \sim 0.7$ and agree with metric-perturbation results [7]; in dCS gravity—in which parity is violated—the slow-rotation master system for $\Psi_{0,4}$ plus the pseudoscalar was derived [14], and the resulting QNM frequency shifts including overtones were computed with cross-gauge (IRG/ORG) and RWZ consistency, and are typically more sensitive to EFT corrections [20]. Moreover, when extra fields couple to curvature, *frequency contamination* leaks additional tones into the gravitational sector [9, 21].

Because EFT effects in astrophysical black holes are expected to be relatively “tiny”, QNM computations require high precision and stringent consistency checks. Given the various avenues for modeling and exploring such beyond-GR imprints (as some summarized above), it is essential to validate both the modified Teukolsky formalism (MTE) framework itself *and* the numerical tools used within. In this work, we establish controlled consistency tests of this kind.

In EFT, several higher-derivative operators are redundant on Ricci-flat backgrounds: using local field redefinitions built from the leading equations of motion, terms proportional to Ricci scalar R , or Ricci tensor $R_{\mu\nu}$, and their derivatives can be removed [1, 22, 23]. In particular, operators with linear Ricci contributions to the EFT-Lagrangian: $R R_{\mu\nu\alpha\beta} R^{\mu\nu\alpha\beta}$ and $R^{\mu\nu} R_{\mu\alpha\beta\gamma} R_{\nu}^{\alpha\beta\gamma}$ do *not* shift asymptotically flat, vacuum observables at

* Corresponding author; mabbasal@buffalo.edu

† mansour@iis.u-tokyo.ac.jp

‡ lehner@perimeterinstitute.ca

§ ds77@buffalo.edu

¶ dongjun@illinois.edu

** pratik.wagle@aei.mpg.de

first order in EFT perturbation parameter ζ —including QNM spectra, excitation factors, scattering amplitudes, and cross sections (see, e.g., [1, 7]). This furnishes a sharp *null test*: we consider such redundant deformations into the QNM computation and verify that the spectrum is not affected up to $\mathcal{O}(\zeta)$, thereby validating the two-parameter bookkeeping (ϵ, ζ) in the modified-Teukolsky program and exposing any spurious numerical contamination. We use this controlled setting to benchmark EVP, and generalized continued fractions with diagnostics focused on truncation systematics and the heightened sensitivity of overtones.

Paper structure. Section II formulates the EFT-modified Teukolsky framework by specifying the Lagrangian, background geometry, and master operator, and discusses axial–polar isospectrality via a corrected superpotential $W(r)$. Section III introduces two independent QNM solvers and their associated diagnostics: the eigenvalue-perturbation (EVP) method (Sec. III A)

and a Leaver-type generalized continued-fraction pipeline (Sec. III B). Numerical results are presented in Sec. IV, and we conclude with a summary and outlook in Sec. V. Explicit EFT effective potentials are collected in Appendix A, while additional implementation details and numerical checks are provided in Appendix B. Full even/odd Frobenius recurrence coefficients are compiled in a companion *Mathematica* notebook and will be made publicly available upon publication.

II. SETUP

We consider the low-energy EFT of gravity in four dimensions, including all parity-even curvature operators of canonical dimension six. We work with signature $(-, +, +, +)$ and natural units $\hbar = c = 1$. Following the conventions of Ref. [1], the dimension-6 part of the Lagrangian is

$$\begin{aligned} \mathcal{L}_{D6} = \frac{\sqrt{-g}}{M^2} & \left[d_1 R \square R + d_2 R_{\mu\nu} \square R^{\mu\nu} + d_3 R^3 + d_4 R R_{\mu\nu} R^{\mu\nu} + d_6 R_{\mu}{}^{\nu} R_{\nu}{}^{\rho} R_{\rho}{}^{\mu} + d_7 R^{\mu\nu} R^{\alpha\beta} R_{\mu\alpha\nu\beta} \right. \\ & \left. + d_5 R R_{\mu\nu\alpha\beta} R^{\mu\nu\alpha\beta} + d_8 R^{\mu\nu} R_{\mu}{}^{\alpha\beta\gamma} R_{\nu\alpha\beta\gamma} + d_9 R_{\mu\nu}{}^{\alpha\beta} R_{\alpha\beta}{}^{\gamma\sigma} R_{\gamma\sigma}{}^{\mu\nu} + d_{10} R_{\mu}{}^{\alpha}{}_{\nu}{}^{\beta} R_{\alpha}{}^{\gamma}{}_{\beta}{}^{\sigma} R_{\gamma}{}^{\mu}{}_{\sigma}{}^{\nu} \right] \\ & \equiv \frac{\sqrt{-g}}{M^2} \sum_{i=1}^{10} d_i \mathcal{O}_i. \end{aligned} \quad (1)$$

where \square is the d'Alembertian operator, $g \equiv \det(g_{\mu\nu})$, d_i are the Wilson coefficients and $R_{\mu\nu\alpha\beta}$ is the Riemann tensor.

On Ricci-flat backgrounds ($R_{\mu\nu} = 0 = R$), operators at least quadratic in R or $R_{\mu\nu}$ (i.e., \mathcal{O}_i with $i = 1, 2, 3, 4, 6, 7$) do not contribute to the background nor to linearized vacuum perturbations at the order we consider. For later convenience we introduce the combination

$$d_{58} \equiv 4d_5 + d_8. \quad (2)$$

The remaining four operators split into two categories: those linear in the Ricci scalar/tensor ($\mathcal{O}_5, \mathcal{O}_8$) and those purely cubic in the Riemann tensor ($\mathcal{O}_9, \mathcal{O}_{10}$). The former are removable by local field redefinitions and, therefore, do not induce first-order QNM shifts in vacuum; in

contrast, the latter are genuinely dynamical and do correct the QNM spectrum at first order. Accordingly, we define two subsets:

- Two *null-test operators*,

$$\begin{aligned} \mathcal{O}_5 &= R R_{\mu\nu\alpha\beta} R^{\mu\nu\alpha\beta}, \\ \mathcal{O}_8 &= R^{\mu\nu} R_{\mu\alpha\beta\gamma} R_{\nu}{}^{\alpha\beta\gamma}, \end{aligned} \quad (3)$$

- Two genuinely *dynamical cubic invariants*,

$$\begin{aligned} \mathcal{O}_9 &= R_{\mu\nu}{}^{\alpha\beta} R_{\alpha\beta}{}^{\gamma\sigma} R_{\gamma\sigma}{}^{\mu\nu}, \\ \mathcal{O}_{10} &= R_{\mu}{}^{\alpha}{}_{\nu}{}^{\beta} R_{\alpha}{}^{\gamma}{}_{\beta}{}^{\sigma} R_{\gamma}{}^{\mu}{}_{\sigma}{}^{\nu}. \end{aligned} \quad (4)$$

Moreover, in four dimensions, \mathcal{O}_{10} is related to \mathcal{O}_9 via the algebraic identity [24]:

$$\mathcal{O}_{10} = \frac{1}{2} \mathcal{O}_9 - \frac{3}{8} \mathcal{O}_5 - 3 R^{\mu\alpha} R^{\nu\beta} R_{\mu\nu\alpha\beta} - 4 R_{\mu}{}^{\nu} R_{\nu}{}^{\rho} R_{\rho}{}^{\mu} + \frac{9}{2} R R_{\mu\nu} R^{\mu\nu} - \frac{5}{8} R^3. \quad (5)$$

In particular, on Ricci-flat backgrounds this reduces to $\mathcal{O}_{10} = \frac{1}{2} \mathcal{O}_9 - \frac{3}{8} \mathcal{O}_5$. Thus, at $\mathcal{O}(\zeta)$ the QNM shift obtained from \mathcal{O}_9 must equal twice the shift from \mathcal{O}_{10} , up

to contamination from the null-test operator \mathcal{O}_5 .

Problem Statement(null tests). Any nonzero QNM shift sourced by \mathcal{O}_5 or \mathcal{O}_8 at $\mathcal{O}(\zeta)$ would indicate a break-

down of our perturbative setup and/or numerical implementation rather than a genuine EFT effect. Also, for equal Wilson coefficients, the ratio of QNM shifts from \mathcal{O}_9 and \mathcal{O}_{10} must be equal to 2 on Ricci-flat backgrounds up to numerical contamination.

Finally, our control (even-parity) sector matches the even-parity cubic operator basis used in Ref. [25]. That reference also considers the (odd-parity) cubic invariant

$$\tilde{\mathcal{O}}_{11} \equiv \frac{1}{2} \epsilon^{\mu\nu\alpha\beta} R_{\mu\nu}{}^{\rho\sigma} R_{\rho\sigma}{}^{\delta\gamma} R_{\delta\gamma\alpha\beta}, \quad (6)$$

For simplicity, we will not consider $\tilde{\mathcal{O}}_{11}$ in this work.

A. Background geometry and master perturbation equations

We work on a static, spherically symmetric background. In Schwarzschild-like coordinates (t, r, θ, ϕ) , the metric takes the form

$$ds^2 = -A(r) dt^2 + \frac{dr^2}{B(r)} + r^2 d\Omega^2, \quad \frac{dr}{d\bar{r}_*} = \sqrt{A(r)B(r)}, \quad (7)$$

where \bar{r}_* is the tortoise coordinate associated with the EFT-deformed background and $d\Omega^2$ is the line element on the unit 2-sphere. We define

$$f(r) \equiv 1 - \frac{r_g}{r}, \quad (8)$$

so that in the GR limit ($\zeta \rightarrow 0$) one has $A(r) = B(r) = f(r)$ and $\bar{r}_* \rightarrow r_*$, where r_* is the standard Schwarzschild tortoise coordinate.

The EFT deformation parameter is

$$\zeta \equiv M^{-2} M_{\text{Pl}}^{-2} r_g^{-4}. \quad (9)$$

At $\mathcal{O}(\zeta)$, the EFT corrections to the background functions $A(r), B(r)$ and the axial/polar potentials can be written in closed form; for completeness we provide the full GR and EFT potentials for both parities in Appendix A.

For odd/even-parity perturbations we adopt the master-equation form of Eq. (2.23) in Ref. [1]:

$$\begin{aligned} \mathcal{L}_{o/e, n\ell}^{(1)} &\equiv \frac{d^2}{d\bar{r}_*^2} + \omega_{n\ell}^2 - \bar{V}_{n\ell}^{o/e}(r; \omega_{n\ell}), \\ \mathcal{L}_{o/e, n\ell}^{(1)} \Psi_{n\ell}^{o/e} &= 0, \end{aligned} \quad (10)$$

where the subscripts (n, ℓ) denote the overtone index and angular multipole, respectively. With effective potentials

$$\begin{aligned} \bar{V}_{n\ell}^{o/e}(r; \omega_{n\ell}) &= \sqrt{A(r)B(r)} \left(V_{n\ell}^{o/e, \text{GR}}(r) + \zeta V_{n\ell}^{o/e}(r) \right) \\ &\quad - \zeta \Delta c(r) \omega_{n\ell}^2. \end{aligned} \quad (11)$$

Note that $V_{n\ell}^{o/e, \text{GR}}(r)$ is ω -independent, whereas the EFT-deformed potential $\bar{V}_{n\ell}^{o/e}(r; \omega)$ depends parametrically on ω ; evaluating it at $\omega = \omega_{n\ell}$ therefore yields mode-dependent effective potentials. The GR piece is related to the standard Regge–Wheeler/Zerilli potentials by

$$V_{n\ell}^{o/e, \text{GR}}(r) = \frac{V_{n\ell}^{\text{RW/Z}}(r)}{f(r)}, \quad (12)$$

while the coefficient of the EFT-induced $\omega_{n\ell}^2$ -term is

$$\Delta c(r) = 144 (2d_9 + d_{10}) \frac{f(r)}{(r/r_g)^5}. \quad (13)$$

B. Axial–polar isospectrality and superpotential

For Schwarzschild in GR ($\zeta = 0$), the odd (axial) and even (polar) sectors are known to be isospectral: for each (ℓ, n) the axial and polar QNM frequencies coincide.

The standard Chandrasekhar transformation relates the RW master and the Zerilli master functions via a superpotential $W_{\text{GR}}(r)$. In our normalization [26, 27],

$$W_{\text{GR}}(r) = \frac{3r_g(r_g - r)}{r^2(3r_g + (\lambda_\ell - 2)r)} - \frac{(\lambda_\ell - 2)\lambda_\ell}{6r_g}, \quad (14)$$

where $\lambda_\ell \equiv \ell(\ell + 1)$.

In the presence of the null-test operators \mathcal{O}_5 and \mathcal{O}_8 , the axial and polar potentials receive EFT corrections, but they remain isospectral to first order in ζ . More precisely, for \mathcal{O}_5 and \mathcal{O}_8 alone the axial and polar sectors continue to be related by a superpotential whose integration constant is unchanged and given by $(2\lambda_\ell - \lambda_\ell^2)/(6r_g)$. The superpotential itself acquires a $\mathcal{O}(\zeta)$ correction:

$$\begin{aligned} W(r) &= W_{\text{GR}}(r) + \zeta d_{58} W_{58}(r), \\ W_{58}(r) &= \frac{9r_g^7(-6r_g^2 - 3rr_g(-3 + \lambda_\ell) + 2r^2(-2 + \lambda_\ell))}{(r^8(3r_g + r(-2 + \lambda_\ell))^2)} \end{aligned} \quad (15)$$

However, while isospectrality between the axial and polar sectors in GR follows from the Chandrasekhar transformation (equivalently, a Darboux/SUSY partner structure of the RW and Zerilli potentials), the corresponding statements in the EFT-deformed problems are more subtle.

It is not straightforward to exhibit an explicit analytic Darboux map that connects the GR spectral problem to the ζ -deformed problems (or, more nontrivially, maps the \mathcal{O}_5 problem to the \mathcal{O}_8 one) in a way that makes these spectral equivalences manifest within the standard Darboux transformation framework [26, 27]. For this reason, we test the expected spectral relations numerically.

The situation changes qualitatively once genuine curvature corrections are switched on through \mathcal{O}_9 and/or \mathcal{O}_{10} : odd/even (parity) isospectrality is then expected to be broken. Indeed, the EFT results of [1] show that the

odd- and even-parity fractional frequency shifts induced by these operators differ, providing explicit numerical evidence that parity isospectrality does not survive in the presence of \mathcal{O}_9 and \mathcal{O}_{10} .

C. Two complementary QNM calculation strategies

We employ two independent approaches to compute the QNM corrections due to the EFT-deformed background: EVP method and Leaver method.

1. EVP method

We follow a two-parameter bookkeeping scheme common in modified Teukolsky and EFT treatments of QNMs. As defined briefly in Sec. I, the parameter ϵ tracks the linear GW perturbation order, while ζ tracks the EFT deformation. We retain terms up to $\mathcal{O}(\zeta^1 \epsilon^1)$ and neglect $\mathcal{O}(\zeta^2)$ corrections.

Expanding the background and fields to first order in ζ we write

$$A(r) = f(r) + \zeta A_1(r), \quad B(r) = f(r) + \zeta B_1(r), \quad (16)$$

$$\sqrt{A(r)B(r)} = f(r) + \zeta \bar{f}(r), \quad \bar{f}(r) \equiv \frac{A_1(r) + B_1(r)}{2}, \quad (17)$$

$$\frac{dr}{d\bar{r}_*} = f(r) + \zeta \bar{f}(r), \quad (18)$$

$$\Psi_{n\ell}^{o/e} = \Psi_{n\ell}^{o/e(0,1)} + \zeta \Psi_{n\ell}^{o/e,(1,1)}, \quad (19)$$

$$\omega_{n\ell} = \omega_{0n\ell} + \zeta \omega_{1n\ell}. \quad (20)$$

Here $\omega_{0n\ell}$ is the GR QNM frequency, and the superscripts (0,1) and (1,1) denote orders $\mathcal{O}(\zeta^0 \epsilon^1)$ and $\mathcal{O}(\zeta^1 \epsilon^1)$, respectively.

Substituting these expansions into Eq. (10) and collecting terms at $\mathcal{O}(\zeta^0 \epsilon^1)$ yields the GR homogeneous problem

$$\mathcal{L}_{o/e,n\ell}^{(0)} \equiv \frac{d^2}{dr_*^2} + \omega_{0n\ell}^2 - f(r) V_\ell^{o/e, \text{GR}}(r), \quad (21)$$

$$\mathcal{L}_{o/e,n\ell}^{(0)} \Psi_{n\ell}^{o/e(0,1)} = 0.$$

At $\mathcal{O}(\zeta^1 \epsilon^1)$ we obtain an inhomogeneous EVP equation of the form

$$\mathcal{L}_{o/e,n\ell}^{(0)} \Psi_{n\ell}^{o/e,(1,1)} = \mathcal{S}_{o/e,n\ell}^{(1,1)} [\Psi_{n\ell}^{o/e(0,1)}; \omega_{1n\ell}], \quad (22)$$

where $\mathcal{S}_{o/e,n\ell}^{(1,1)}$ encodes all EFT-induced source terms built from the GR background, the GR eigenfunction $\Psi_{n\ell}^{o/e(0,1)}$, and the frequency correction $\omega_{1n\ell}$.

We extract $\omega_{1n\ell}$ by using the bilinear form that renders $\mathcal{L}_{o/e,n\ell}^{(0)}$ formally self-adjoint under the appropriate QNM

inner product. Schematically,

$$\begin{aligned} \omega_{1n\ell} &= - \frac{\langle \Psi_{n\ell}^{o/e(0,1)} | \delta \mathcal{L}_{o/e,n\ell}^{(1)} [\Psi_{n\ell}^{o/e(0,1)}] \rangle}{\langle \Psi_{n\ell}^{o/e(0,1)} | \partial_\omega \mathcal{L}_{o/e,n\ell}^{(0)}(\omega_{0n\ell}) \Psi_{n\ell}^{o/e(0,1)} \rangle} \\ &\equiv \frac{N_{o/e}}{D_{o/e}} \end{aligned} \quad (23)$$

where $\delta \mathcal{L}_{o/e,n\ell}^{(1)}$ is the $\mathcal{O}(\zeta)$ EFT correction to the master operator, and the numerator and denominator $N_{o/e}, D_{o/e}$ are implemented as contour integrals over the complex r -plane in our EVP approach. The detailed contour representation of the bilinear form, and its numerical discretization, are described in Sec. III A.

2. Scalar Leaver method on the EFT master equation

For the EFT-corrected master operator in Eq. (10), the effective potentials $\bar{V}_{n\ell}^{o/e}(r; \omega)$ vanish near r_H . At spatial infinity they decay with the same asymptotic behaviour as in GR. Consequently, the asymptotic solutions still behave as $e^{\pm i\omega \bar{r}_*}$, and we impose standard black hole boundary conditions: purely ingoing waves at the perturbed horizon r_H and purely outgoing waves as $r \rightarrow \infty$.

The perturbed horizon radius is defined as the common positive root of $A(r) = B(r) = 0$. To linear order in ζ we write

$$r_H = r_g \beta, \quad \beta = 1 - \zeta \left(3d_{58} + 10d_9 + \frac{1}{2}d_{10} \right), \quad (24)$$

and introduce the EFT-corrected surface-gravity radius

$$\frac{1}{2\kappa} \equiv r_{\text{SG}} \equiv r_g (1 - 2(d_{10} + 2d_9)\zeta), \quad (25)$$

which controls the phase of the near-horizon behaviour.

Following Leaver [18], we peel off the non-analytic asymptotics at the horizon and at infinity with the ansatz

$$\Psi_{n\ell}^{o/e}(r) = \phi(r) \tilde{\Psi}_{n\ell}^{o/e}(r), \quad (26)$$

where

$$\phi(r) = (r - r_H)^{-i\omega r_{\text{SG}}} e^{i\omega(r - r_H)} \left(\frac{r}{r_H} \right)^{i\omega(r_g + r_{\text{SG}})}. \quad (27)$$

Here and throughout, when it is unambiguous we suppress some mode labels (typically n and/or ℓ) for notational clarity. We reinstate the full index set whenever needed. By construction, $\phi(r)$ enforces the boundary conditions. The remaining factor $\tilde{\Psi}_{n\ell}^{o/e}(r)$ is analytic at $r = r_H$ and can be expanded in a Frobenius series. Introducing the dimensionless radial coordinate

$$x \equiv 1 - \frac{r_H}{r}, \quad (28)$$

we write

$$\tilde{\Psi}_{n\ell}^{o/e}(r) = \sum_{m=0}^{\infty} a_m^{o/e} x^m, \quad (29)$$

with $a_0^{o/e}$ fixed by normalization.

Substituting Eqs. (26)–(29) into the master equation (10) and expanding about $x = 0$ gives, for each parity sector, a linear recurrence for the coefficients $a_m^{o/e}$. For the even and odd sectors we obtain, respectively,

$$\sum_{k=-10}^{+1} \Gamma_k^{(e)}(m) a_{m+k}^{(e)} = 0, \quad (30)$$

$$\sum_{k=-7}^{+1} \Gamma_k^{(o)}(m) a_{m+k}^{(o)} = 0, \quad (31)$$

where m is the Frobenius index. The coefficients $\Gamma_k^{(e/o)}(m)$ are at most quadratic polynomials in m , lin-

ear in ζ and in the couplings $\{d_5, d_8, d_9, d_{10}\}$, and they depend on the frequency $\omega_{n\ell}$ and on the angular index ℓ . Explicit expressions for all $\Gamma_k^{(e/o)}(m)$ are compiled in a companion *Mathematica* notebook and will be made publicly available upon publication.

These “fat” m -band recurrences (with $m = 12$ for even and $m = 9$ for odd) could in principle be treated using Hill determinants or a tensorial generalization of Leaver’s continued-fraction method [28–31]. Instead, we perform an exact numerical band reduction from the m -term system to an equivalent 3-term recurrence of the form

$$\tilde{\alpha}(m) a_{m-1} + \tilde{\beta}(m) a_m + \tilde{\gamma}(m) a_{m+1} = 0, \quad (32)$$

for both parity sectors. Here, $(\tilde{\alpha}(m), \tilde{\beta}(m), \tilde{\gamma}(m))$ labels the 3-term band coefficients after reduction.

We then solve for the minimal solution using a scalar Leaver continued-fraction algorithm [18]. Implementation details and numerical checks are discussed in Sec. III B (see also Appendix B).

TABLE I. Fractional shifts using EVP method δ_{EVP} for (n, ℓ) with $\ell = 2$. In each data cell, the top row corresponds to the even sector and the bottom row to the odd sector. The left and right entries are $\Re(\delta_{\text{EVP}})$ and $\Im(\delta_{\text{EVP}})$ respectively.

		(0, 2)		(1, 2)		(2, 2)		(3, 2)	
\mathcal{O}_5	<i>even</i>	3.42×10^{-18}	-1.84×10^{-17}	-8.18×10^{-14}	-3.64×10^{-14}	4.88×10^{-11}	5.60×10^{-11}	1.04×10^{-8}	-1.88×10^{-9}
	<i>odd</i>	2.23×10^{-18}	-1.18×10^{-17}	-5.39×10^{-14}	-1.85×10^{-14}	4.03×10^{-11}	3.34×10^{-11}	6.34×10^{-9}	-1.88×10^{-9}
\mathcal{O}_8	<i>even</i>	8.55×10^{-19}	-4.60×10^{-18}	-2.04×10^{-14}	-9.10×10^{-15}	1.22×10^{-11}	1.40×10^{-11}	2.60×10^{-9}	-4.71×10^{-10}
	<i>odd</i>	5.57×10^{-19}	-2.94×10^{-18}	-1.35×10^{-14}	-4.63×10^{-15}	1.01×10^{-11}	8.35×10^{-12}	1.59×10^{-9}	-4.69×10^{-10}
\mathcal{O}_9	<i>even</i>	12.34	58.12	-10.76	55.82	-75.80	54.48	-229.39	61.44
	<i>odd</i>	-21.07	-47.53	-16.36	-70.57	51.79	-115.18	392.92	-183.67
\mathcal{O}_{10}	<i>even</i>	6.17	29.06	-5.38	27.91	-37.90	27.24	-114.70	30.72
	<i>odd</i>	-10.54	-23.76	-8.18	-35.29	25.90	-57.59	196.46	-91.83

TABLE II. Fractional shifts δ_{EVP} for (n, ℓ) with $\ell = 3$. Layout as in the $\ell = 2$ table.

		(0, 3)		(1, 3)		(2, 3)		(3, 3)	
\mathcal{O}_5	<i>even</i>	1.50×10^{-23}	5.02×10^{-23}	3.38×10^{-20}	1.95×10^{-19}	1.99×10^{-17}	1.64×10^{-16}	3.35×10^{-14}	3.95×10^{-14}
	<i>odd</i>	1.46×10^{-23}	3.45×10^{-23}	4.50×10^{-20}	1.70×10^{-19}	4.42×10^{-17}	1.50×10^{-16}	4.37×10^{-14}	3.27×10^{-14}
\mathcal{O}_8	<i>even</i>	3.76×10^{-24}	1.26×10^{-23}	8.45×10^{-21}	4.88×10^{-20}	4.97×10^{-18}	4.11×10^{-17}	8.37×10^{-15}	9.89×10^{-15}
	<i>odd</i>	3.66×10^{-24}	8.62×10^{-24}	1.13×10^{-20}	4.24×10^{-20}	1.10×10^{-17}	3.74×10^{-17}	1.09×10^{-14}	8.17×10^{-15}
\mathcal{O}_9	<i>even</i>	14.15	51.82	7.99	53.53	-8.03	57.09	-42.34	62.89
	<i>odd</i>	-18.29	-46.27	-15.65	-51.39	-5.25	-61.31	25.14	-75.63
\mathcal{O}_{10}	<i>even</i>	7.07	25.91	4.00	26.77	-4.02	28.55	-21.17	31.44
	<i>odd</i>	-9.14	-23.13	-7.82	-25.70	-2.63	-30.65	12.57	-37.82

III. NUMERICAL METHODS

In Ref. [1], QNM shifts were evaluated using a frequency-basis expansion in which the EFT-induced po-

tential deformation is written asymptotically as

$$\delta V = r_H^{-2} \sum_{j \geq 0} z_j (r_H/r)^j, \quad (33)$$

TABLE III. Fractional shifts δ_{EVP} for (n, ℓ) with $\ell = 4$. Layout as in the $\ell = 2$ table.

		(0, 4)		(1, 4)		(2, 4)		(3, 4)	
\mathcal{O}_5	<i>even</i>	-1.25×10^{-27}	-1.05×10^{-26}	5.77×10^{-24}	-4.42×10^{-24}	6.38×10^{-22}	1.01×10^{-20}	-2.18×10^{-18}	9.44×10^{-19}
	<i>odd</i>	-1.36×10^{-27}	-9.11×10^{-27}	5.48×10^{-24}	-6.36×10^{-24}	1.50×10^{-21}	9.84×10^{-21}	-2.06×10^{-18}	1.31×10^{-18}
\mathcal{O}_8	<i>even</i>	-3.13×10^{-28}	-2.63×10^{-27}	1.44×10^{-24}	-1.10×10^{-24}	1.60×10^{-22}	2.51×10^{-21}	-5.45×10^{-19}	2.36×10^{-19}
	<i>odd</i>	-3.41×10^{-28}	-2.28×10^{-27}	1.37×10^{-24}	-1.59×10^{-24}	3.75×10^{-22}	2.46×10^{-21}	-5.14×10^{-19}	3.28×10^{-19}
\mathcal{O}_9	<i>even</i>	14.46	50.16	11.45	51.35	4.28	53.74	-9.49	57.39
	<i>odd</i>	-17.55	-45.70	-15.80	-47.80	-11.07	-51.93	-0.56	-58.02
\mathcal{O}_{10}	<i>even</i>	7.23	25.08	5.72	25.68	2.14	26.87	-4.75	28.70
	<i>odd</i>	-8.77	-22.85	-7.90	-23.90	-5.53	-25.96	-0.28	-29.01

so that, at linear order, the QNM frequency can be expressed as

$$\omega = \omega_0 + \sum_{j \geq 0} z_j e_j, \quad (34)$$

where δV represents the $\mathcal{O}(\zeta)$ deformation of the master potential (in our notation, the ζ -dependent part of \bar{V}). Here the complex coefficients e_j are precomputed numerically for each ℓ and (in practice) provided up to a finite cutoff j_{max} (e.g. $j_{\text{max}} = 50$ in the implementation used in Ref. [1], following [32]) and z_j are the corresponding expansion coefficients.

This strategy is efficient for estimating physical shifts, but two systematics become critical for *null* cases where the numerical floor is the answer. First, for even-parity perturbations the far-zone series contains infinitely many terms, so truncating the sum at finite j_{max} generically leaves a residual that can dominate the numerical floor (for instance, Ref. [1] estimates an even-parity truncation floor of order $\mathcal{O}(10^{-3})$ for $\ell = 2$ when $j_{\text{max}} = 50$); by contrast, the odd-parity deformation is a finite polynomial in r_H/r in the cases of interest, so null residuals are not truncation-dominated. Second, because e_j are numerically tabulated at finite precision, their use imposes an intrinsic roundoff floor: null results are cancellation-dominated residuals, and any finite-precision error in a_j and/or e_j can propagate into an apparent nonzero $\delta\omega$.

The key practical difference in our approach is that we do not rely on a truncated far-zone power-law expansion calibrated by fixed tabulated coefficients. Instead, we solve the (perturbative) eigenvalue problem directly using arbitrary-precision arithmetic and independent numerical approaches (EVP and generalized Leaver-type continued fractions), and we quantify the numerical floor by systematic convergence under increased precision and tightened truncation controls. This is essential for establishing robust tests for null operators.

In this section we summarize the two numerical approaches used in this work.

A. EVP method

The EVP approach proceeds as follows:

1. compute the GR QNM frequency $\omega_{0n\ell}$ and series coefficients using a continued fraction with a Nollert-type asymptotic tail [18, 33–36], see App. B 1 for more details;
2. reconstruct the RW and Zerilli (as well as Teukolsky functions for cross-check) on a complex r -contour, using branch-tracked prefactors. See implementation details in App. B 2;
3. evaluate a contour bilinear form to obtain the first-order frequency shift $\omega_{1n\ell}$ due to the EFT source operators, see Sec. II for EVP expressions.

a. Complex contour and Chandrasekhar map. The EVP bilinear form is evaluated along a complex r -contour \mathcal{C} . It is convenient to parameterize this contour by a real parameter $\lambda \in [-\lambda_{\text{max}}, \lambda_{\text{max}}]$. We introduce a dimensionless coordinate

$$\rho(\lambda) \equiv \frac{r(\lambda)}{r_g} = 1 + \frac{\lambda}{1 + \lambda^2} + i(\lambda^2 - 2). \quad (35)$$

For large $|\lambda|$ the contour extends to $\text{Im } r \rightarrow +\infty$. It crosses the real axis at $\lambda = \pm\sqrt{2}$ and reaches its minimum imaginary part at $\lambda = 0$, where $\text{Im } r = -2r_g$. The derivative $dr/d\lambda$ is computed spectrally on the λ -grid and is used both in the quadrature weights and in propagating the branch-tracked prefactors.

The Zerilli function $\Psi^{e(0,1)}$ is obtained via the Chandrasekhar transformation built from the GR superpotential $W_{\text{GR}}(r)$ in Eq. (14).

b. Bilinear form and normalization denominator. For each parity sector we define the EVP denominator as

$$D_{o/e} = \oint_{\mathcal{C}} 2\omega_0 [\psi_{\text{GR}}^{o/e}(r)]^2 dr_*, \quad (36)$$

where the QNM inner product is understood in the sense of complex contour integration. Parameterizing the con-

tour by λ , we write

$$\frac{dr_*}{d\lambda} = \frac{1}{f(r(\lambda))} \frac{dr}{d\lambda} \equiv w_r(\lambda), \quad (37)$$

and approximate the integral by a trapezoidal rule on a uniform λ -grid:

$$D_{o/e} \simeq \sum_i 2\omega_0 (\psi_{\text{GR}}^{o/e})_i^2 w_{r,i} \Delta\lambda, \quad (38)$$

with $w_{r,i} = w_r(\lambda_i)$.

The numerator $N_{o/e}$ is evaluated similarly. The integrand is assembled pointwise on the contour using the RW/Zerilli/Teukolsky fields and their radial derivatives.

1. EVP Discretization choices and convergence

The EVP contour integrals are computed on a uniform grid in $\lambda \in [-\lambda_{\text{max}}, \lambda_{\text{max}}]$ with $\lambda_{\text{max}} = 5$, using $N_\lambda = 2000$ sampling points and a trapezoidal rule for all contour integrals.

For the Frobenius expansions of both the RW and Teukolsky solutions we use $N_{\text{max}} = 900$ terms. The continued fraction for the GR problem is evaluated with a Nollert-type asymptotic tail, with base index $N_{\text{tail}} = 700$, step $\Delta N = 60$, and exponent $p = \frac{1}{2}$. We have also checked that slightly deeper tails (for instance $N_{\text{tail}} = 800$, $\Delta N = 100$) do not change the results within the quoted digits.

All EVP runs use high-precision arithmetic with 100 digits, and the GR QNM roots are converged to a tolerance $|\delta\omega| \lesssim 10^{-30}$. As a sanity check we evaluate the GR residuals on a real radial grid $r \in [r_g + 10^{-5}, 100 r_g]$ with $\mathcal{O}(10^2)$ points (for example $N_r \simeq 160$), and verify that the residual ∞ -norm remains small and stable under reasonable variations of N_{max} , $(-\lambda_{\text{max}}, \lambda_{\text{max}}, N_\lambda)$, and $(N_{\text{tail}}, \Delta N, p)$.

B. Leaver method + band reduction

Our second approach provides an independent cross-check by solving the fully EFT-corrected recurrence directly, without contour integration. We use a band-reduced Leaver solver¹. The implementation proceeds in two main steps:

¹ Our implementation follows the logic of the public `qnm` package [37], but is reimplemented end-to-end in `mpmath`, together with an additional reduction step that handles the m -term banded recurrences that arise in the modified equations. This enables arbitrary-precision complex arithmetic and allows us to push the numerical floor tests well below that of `qnm`. By contrast, `qnm` is optimized for speed using `numpy` and `numba` [37], which operate at machine precision, whereas `mpmath` targets arbitrary precision. The tradeoff is increased runtime that grows with the requested precision and reduced benefit from low-level vectorization speedups; we overcome those cons by parallelizing over different cores and caching roots.

1. *Reduce to a three-term recurrence.* We perform an exact numerical band reduction, via banded Gaussian elimination, from the m -term recurrences to an equivalent 3-term recurrence.
2. *Evaluate the continued fraction and find the root.* We apply a scalar Leaver continued-fraction solver to the reduced recurrence, using a modified Lentz's method [38, 39] for the infinite tail and a complex secant-Newton root finder for ω_{nl} .

For a chosen inversion index $m_{\text{inv}} \geq 1$, we write the spectral function as

$$F(\omega) = \tilde{\beta}_{m_{\text{inv}}} - \tilde{\gamma}_{m_{\text{inv}}} C_{m_{\text{inv}}-1}(\omega) + \tilde{\gamma}_{m_{\text{inv}}} T_{m_{\text{inv}}}(\omega), \quad (39)$$

where $C_{m_{\text{inv}}-1}$ is the contribution from the finite prefix of the continued fraction down to $m = 0$, and $T_{m_{\text{inv}}}$ is the infinite tail starting at m_{inv} .

The finite prefix is computed recursively as

$$C_{-1} = 0, \quad C_k = \frac{\tilde{\alpha}_k}{\tilde{\beta}_k - \tilde{\gamma}_k C_{k-1}}, \quad k = 0, 1, \dots, m_{\text{inv}}-1. \quad (40)$$

The tail $T_{m_{\text{inv}}}$ is evaluated using a modified Lentz algorithm for the associated J -fraction. In terms of the tri-diagonal coefficients, we define

$$A_j = -\frac{\tilde{\alpha}_{m_{\text{inv}}+j}}{\tilde{\gamma}_{m_{\text{inv}}+j}}, \quad B_j = \frac{\tilde{\beta}_{m_{\text{inv}}+j+1}}{\tilde{\gamma}_{m_{\text{inv}}+j+1}}, \quad (41)$$

and iterate the standard Lentz update for f_j , C_j , D_j and Δ_j until the fractional change falls within the chosen tolerance. This yields an evaluation of $F(\omega)$ together with a tail error estimate $\varepsilon_{\text{tail}}$.

To better align the inversion index with the minimal solution of the recurrence, we perform a cheap ‘‘neighbor-pick’’ step: given a seed m_{inv} , we briefly evaluate $|F(\omega)|$ for a small window of neighboring inversion indices and choose the one that minimizes $|F(\omega)|$. This step is inexpensive and improves the robustness of the solver.

The core QNM condition $F(\omega) = 0$ is solved using a complex secant method with an optional Newton polish. Starting from two jittered seeds ω_{0nl} and ω_{1nl} around a reference frequency ω_{seed} , we iterate

$$\omega_{k+1} = \omega_k - F(\omega_k) \frac{\omega_k - \omega_{k-1}}{F(\omega_k) - F(\omega_{k-1})}, \quad (42)$$

until $|F(\omega_k)|$ falls below a target root tolerance. If the secant denominator becomes too small, we temporarily switch to a single Newton step with a numerically estimated derivative,

$$F'(\omega) \approx \frac{F(\omega + h) - F(\omega - h)}{2h}, \quad (43)$$

where h is chosen adaptively based on the target precision and $|\omega|$. After the secant phase, we perform one additional Newton polish on the final iterate.

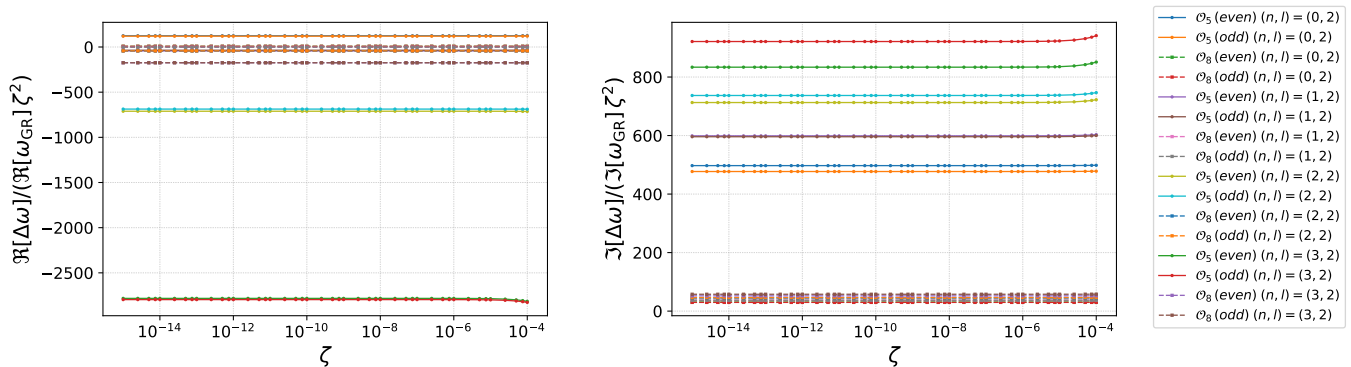


FIG. 1. Scaling test of the EFT-induced frequency shift for \mathcal{O}_5 and \mathcal{O}_8 at $\ell = 2$. The left (right) panel shows the real (imaginary) part of the reduced quantity $\delta_{\text{Leaver}}/\zeta^2$ as a function of the coupling ζ . The near-constancy of these curves over a wide range of ζ indicates that the leading correction scales quadratically, $\delta_{\text{Leaver}} \propto \zeta^2$. Deviations from flatness at the largest couplings signal the onset of non-asymptotic (higher-order) contributions beyond the leading power.

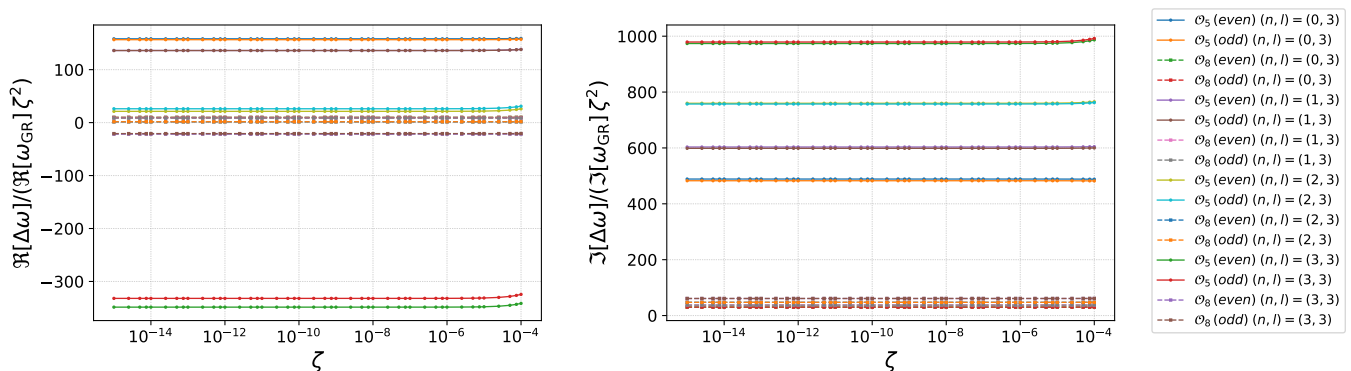


FIG. 2. Same as Fig. 1 but for $\ell = 3$.

We estimate the uncertainty $\delta\omega$ in the extracted frequency by combining the nonlinear root-finding residual and the tail truncation error. Defining $F_{\text{residual}}(\omega) \equiv F(\omega)$, evaluated at the final iterate, we use

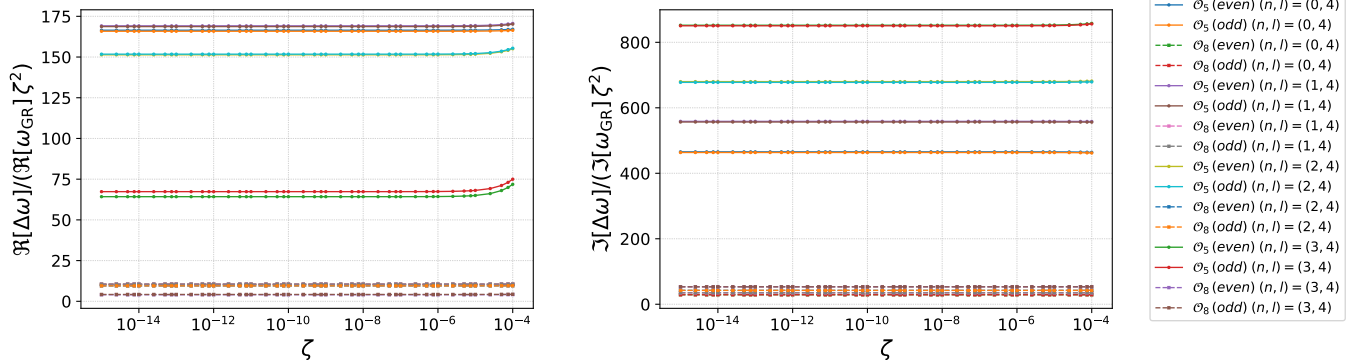
$$\delta\omega \sim \frac{|F_{\text{residual}}(\omega)| + \varepsilon_{\text{tail}}}{|F'(\omega)|}. \quad (44)$$

This provides a conservative internal error estimate for the Leaver+reduction solver, which we compare against the EVP results and the expected null-test behaviour of \mathcal{O}_5 and \mathcal{O}_8 .

1. Leaver Discretization choices and convergence

All runs use 80 digits high-precision arithmetic, and strict continued-fraction and root-finding tolerances set to 10^{-60} . The reduced tridiagonal recurrence starts from an initial depth of 10^4 and is allowed to grow up to a ceiling of 2.5×10^5 with a multiplicative growth factor of 1.6. The solver can also shrink the working depth again when a significant fraction of the array is unused, effectively reducing the depth once more than about 40% of the current depth is not needed.

For each mode, the initial guess is taken once from the tabulated Schwarzschild spectrum provided by the `qnm` library and a second time from a simple eikonal estimate, in order to compare robustness against different seed choices. The root finder uses a complex secant method followed by up to 3 Newton iterations. The effective convergence threshold on the residual is defined as the maximum of the nominal root tolerance, a floor tied to the continued-fraction truncation error, and the intrinsic precision floor, which is approximately 10^{-78} .

FIG. 3. Same as Fig. 1 but for $\ell = 4$.

IV. NUMERICAL RESULTS

In this section, we present QNM shifts for overtones $n = 0, 1, 2, 3$ and multipoles $\ell = 2, 3, 4$ in both even and odd sectors. We work in units $r_g = 1$ throughout, so that the $n = 0$ modes can be compared directly with results of Ref. [1].

A. EVP

Using the EVP approach on the λ -contour described in Sec. III A, we compute the first-order fractional shifts δ_{EVP} for all modes in our grid. Following Eq. (4.7) of Ref. [1], we report the dimensionless *fractional shift*

$$\delta_{\text{EVP}} \equiv \left(\frac{\Re(\omega_1)}{\Re(\omega_0)}, \frac{\Im(\omega_1)}{\Im(\omega_0)} \right). \quad (45)$$

The numerical values are reported in Tables I, II and III.

1. Null operators

In theory, for the null operators \mathcal{O}_5 and \mathcal{O}_8 , the linear response of the spectrum in vacuum should vanish. Analyzing δ_{EVP} for all ℓ and n , we find

$$\begin{aligned} |\delta_{\text{EVP},\text{min}}| &\sim 10^{-28}, \\ |\delta_{\text{EVP},\text{median}}| &\sim 10^{-18}, \\ |\delta_{\text{EVP},\text{max}}| &\lesssim 10^{-8}. \end{aligned} \quad (46)$$

The even and odd sectors show the same qualitative behaviour, with the odd sector differing only by factors of order unity.

Two systematic trends are apparent. First, at fixed ℓ , $|\delta_{\text{EVP}}^{(5,8)}|$ increases as one moves to higher overtones n . Second, at fixed overtone n , $|\delta_{\text{EVP}}^{(5,8)}|$ decreases as ℓ increases. In other words, the largest deviations from the ideal null

result occur in the corner of the grid ($\ell = 2, n = 3$), while higher- ℓ fundamentals are closest to zero.

The first pattern is consistent with the fact that higher overtones are intrinsically more challenging: they are more sensitive to root-finding errors, and small inaccuracies in ω_0 propagate into the reconstruction of the scalar fields and the contour integrals, leading to cumulative systematic errors. We do not attempt to separate these contributions in detail here; instead we interpret the observed $|\delta_{\text{EVP}}^{(5,8)}|$ as a practical measure of the numerical floor of the EVP method.

It is instructive to compare with the results of Ref. [1] that uses method developed in [32] to compute the QNMs. They have focused on the fundamental modes ($n = 0$) with $\ell = 2, 3, 4$ and reported maximal null-operator shifts of order 10^{-4} in the even sector and 10^{-6} in the odd sector. Over the same set of modes, our EVP implementation reduces these residuals by several orders of magnitude, yielding $|\delta_{\text{EVP}}| \lesssim 10^{-17}$ while simultaneously extending the null test to overtones up to $n = 3$ without loss of control. We speculate that the improvement is primarily due to avoiding the series truncation error used in Ref. [1] and [32]: in EVP we compute the shift directly from the perturbed eigenvalue problem at high precision, and verify convergence so the residual in null cases is driven down to a much lower numerical floor.

2. Control Operators

Up to an overall sign (that can be traced to a difference in conventions), the EVP results for \mathcal{O}_9 and \mathcal{O}_{10} operators gives a fractional shifts δ_{EVP} are $\mathcal{O}(10^0 - 10^2)$. They agree with those of Ref. [1] in magnitude for both the real and imaginary parts upon rounding to the two decimal places reported in their Table I.

Moreover, across all ratios between ω_1 due to \mathcal{O}_9 to \mathcal{O}_{10} are essentially 2, again with maximum absolute deviation observed is $\max |\mathcal{R}_{9/10} - 2| \sim 10^{-11}$. Generally, the deviation was increasing with higher overtone.

TABLE IV. Power-scaling summary for $\zeta_{\max} = 10^{-3}$, odd parity, and null operators. Each p entry is $p_{\text{eff}} \pm \sigma_p$ with the chosen discrete p_* shown as $[p_*]$. C lists the fitted coefficient components $\Re(C) | \Im(C)$ and σ/μ is the flatness ratio.

ℓ	n	\mathcal{O}_5			\mathcal{O}_8		
		p	C	σ/μ	p	C	σ/μ
2	0	2.0002 ± 0.0007 [2]	121.79 479.64	1.08×10^{-3}	2.0001 ± 0.0002 [2]	7.52 29.86	2.72×10^{-4}
2	1	2.0006 ± 0.0019 [2]	-31.52 605.84	2.96×10^{-3}	2.0001 ± 0.0005 [2]	-2.17 37.40	7.33×10^{-4}
2	2	2.0007 ± 0.0023 [2]	-690.29 761.17	3.99×10^{-3}	2.0002 ± 0.0006 [2]	-43.01 46.43	9.83×10^{-4}
2	3	2.0010 ± 0.0034 [2]	-2872.44 971.75	5.11×10^{-3}	2.0003 ± 0.0009 [2]	-175.94 58.34	1.26×10^{-3}
3	0	1.9999 ± 0.0002 [2]	158.36 481.01	7.61×10^{-4}	2.0000 ± 0.0001 [2]	9.82 30.14	1.86×10^{-4}
3	1	2.0002 ± 0.0008 [2]	141.23 601.60	1.60×10^{-3}	2.0001 ± 0.0002 [2]	8.59 37.46	4.01×10^{-4}
3	2	2.0006 ± 0.0020 [2]	38.11 769.90	3.79×10^{-3}	2.0002 ± 0.0005 [2]	1.82 47.53	9.38×10^{-4}
3	3	2.0008 ± 0.0027 [2]	-312.50 1011.00	5.94×10^{-3}	2.0002 ± 0.0007 [2]	-20.46 61.69	1.45×10^{-3}
4	0	1.9998 ± 0.0007 [2]	167.22 459.85	1.29×10^{-3}	1.9999 ± 0.0002 [2]	10.39 28.91	3.17×10^{-4}
4	1	2.0000 ± 0.0000 [2]	172.36 555.50	1.09×10^{-3}	2.0000 ± 0.0000 [2]	10.60 34.77	2.69×10^{-4}
4	2	2.0003 ± 0.0009 [2]	160.86 681.24	2.33×10^{-3}	2.0001 ± 0.0002 [2]	9.63 42.41	5.80×10^{-4}
4	3	2.0006 ± 0.0021 [2]	86.46 864.01	4.53×10^{-3}	2.0002 ± 0.0005 [2]	4.50 53.37	1.12×10^{-3}

TABLE V. Power-scaling summary for $\zeta_{\max} = 10^{-3}$, even parity, and null operators. Layout as in IV.

ℓ	n	\mathcal{O}_5			\mathcal{O}_8		
		p	C	σ/μ	p	C	σ/μ
2	0	2.0002 ± 0.0007 [2]	126.58 499.91	1.09×10^{-3}	2.0001 ± 0.0002 [2]	7.81 31.12	2.74×10^{-4}
2	1	2.0006 ± 0.0019 [2]	-39.11 609.46	3.08×10^{-3}	2.0001 ± 0.0005 [2]	-2.64 37.60	7.64×10^{-4}
2	2	2.0007 ± 0.0024 [2]	-716.55 736.74	4.02×10^{-3}	2.0002 ± 0.0006 [2]	-44.53 44.92	9.89×10^{-4}
2	3	2.0011 ± 0.0036 [2]	-2863.94 877.71	5.24×10^{-3}	2.0003 ± 0.0009 [2]	-175.17 52.77	1.29×10^{-3}
3	0	1.9999 ± 0.0002 [2]	160.04 486.96	7.76×10^{-4}	2.0000 ± 0.0001 [2]	9.92 30.52	1.89×10^{-4}
3	1	2.0002 ± 0.0008 [2]	141.43 606.48	1.63×10^{-3}	2.0001 ± 0.0002 [2]	8.59 37.76	4.08×10^{-4}
3	2	2.0006 ± 0.0020 [2]	33.12 772.96	3.83×10^{-3}	2.0002 ± 0.0005 [2]	1.51 47.70	9.47×10^{-4}
3	3	2.0008 ± 0.0027 [2]	-330.29 1005.92	5.87×10^{-3}	2.0002 ± 0.0007 [2]	-21.51 61.36	1.43×10^{-3}
4	0	1.9998 ± 0.0007 [2]	167.87 461.82	1.31×10^{-3}	1.9999 ± 0.0002 [2]	10.43 29.04	3.21×10^{-4}
4	1	2.0000 ± 0.0000 [2]	172.87 557.51	1.09×10^{-3}	2.0000 ± 0.0000 [2]	10.63 34.90	2.70×10^{-4}
4	2	2.0003 ± 0.0009 [2]	160.51 683.69	2.34×10^{-3}	2.0001 ± 0.0002 [2]	9.60 42.56	5.84×10^{-4}
4	3	2.0006 ± 0.0021 [2]	83.30 865.99	4.54×10^{-3}	2.0002 ± 0.0005 [2]	4.30 53.48	1.12×10^{-3}

Finally, we stress that the EVP computation only probes the linear response of the spectrum, encoded in the first-order coefficients ω_1 and hence in δ_{EVP} . By construction, this method cannot determine the range in

which the expansion

$$\omega(\zeta) = \omega_0 + \zeta \omega_1 + \zeta^2 \omega_2 + \mathcal{O}(\zeta^3) \quad (47)$$

is well-approximated by its linear truncation.

B. Leaver method + band reduction

Now we compute the EFT-corrected frequency $\omega(\zeta)$ for some values $\zeta = \alpha 10^{-p}$ with $p \in \{3, 4, \dots, 15\}$ and $\alpha \in \{1, \frac{3}{4}, \frac{1}{2}, \frac{1}{4}\}$, keeping only $\zeta \in [10^{-15}, 10^{-3}]$.

a. EFT validity and choice of ζ range. The EFT linear expansion in ζ is only meaningful as long as the background is not strongly deformed. An out-of-envelope diagnostic is the correction to the horizon radius r_H . For example, we find that at $d_5 \zeta = 10^{-2}$ the horizon is shifted by about 12% from r_g , while for $d_9 \zeta = 10^{-2}$ the shift is

about 10%.² To remain safely within the linear regime, in what follows we therefore take $\zeta_{\max} = 10^{-4}$ as our default upper limit, and treat $\zeta = 10^{-3}$ only as a reference point illustrating the onset of linear perturbation failure³.

² Pushing to $d_i \zeta = 10^{-1}$ is not even physically meaningful, since r_H would formally become negative.

³ In what follows, Wilson coefficients $d_i \in \{0, 1\}$ is a switch that selects the i th EFT operator, while ζ is the explicit perturbation parameter.

TABLE VI. Power-scaling summary for $\zeta_{\max} = 10^{-3}$, odd parity, and control operators. Layout as in IV.

ℓ	n	\mathcal{O}_9			\mathcal{O}_{10}		
		p	C	σ/μ	p	C	σ/μ
2	0	0.9992 ± 0.0027 [1]	21.25 46.31	4.54×10^{-3}	0.9997 ± 0.0011 [1]	10.53 23.54	1.66×10^{-3}
2	1	0.9999 ± 0.0006 [1]	20.40 69.28	1.12×10^{-2}	0.9997 ± 0.0009 [1]	8.95 34.85	4.66×10^{-3}
2	2	1.0015 ± 0.0049 [1]	-16.24 129.38	5.74×10^{-2}	1.0004 ± 0.0012 [1]	-18.80 60.84	2.35×10^{-2}
2	3	0.9896 ± 0.0568 [1]	-58.05 284.37	1.54×10^{-1}	0.9982 ± 0.0126 [1]	-162.20 124.76	4.11×10^{-2}
3	0	0.9991 ± 0.0031 [1]	18.35 45.04	4.74×10^{-3}	0.9997 ± 0.0010 [1]	9.13 22.94	1.49×10^{-3}
3	1	0.9989 ± 0.0038 [1]	16.52 49.59	7.16×10^{-3}	0.9994 ± 0.0020 [1]	7.92 25.26	3.18×10^{-3}
3	2	0.9999 ± 0.0010 [1]	10.54 60.32	1.68×10^{-2}	0.9997 ± 0.0012 [1]	3.65 30.29	6.80×10^{-3}
3	3	1.0011 ± 0.0031 [1]	-5.21 81.24	4.95×10^{-2}	1.0001 ± 0.0003 [1]	-8.51 39.02	2.03×10^{-2}
4	0	0.9991 ± 0.0031 [1]	17.57 44.51	4.68×10^{-3}	0.9997 ± 0.0009 [1]	8.76 22.68	1.34×10^{-3}
4	1	0.9988 ± 0.0041 [1]	16.13 46.10	6.62×10^{-3}	0.9995 ± 0.0018 [1]	7.91 23.54	2.71×10^{-3}
4	2	0.9988 ± 0.0043 [1]	12.90 49.84	1.00×10^{-2}	0.9993 ± 0.0024 [1]	5.82 25.42	4.43×10^{-3}
4	3	0.9996 ± 0.0020 [1]	7.06 56.95	2.18×10^{-2}	0.9996 ± 0.0016 [1]	1.57 28.64	8.89×10^{-3}

TABLE VII. Power-scaling summary for $\zeta_{\max} = 10^{-3}$, even parity, and control operators. Layout as in IV.

ℓ	n	\mathcal{O}_9			\mathcal{O}_{10}		
		p	C	σ/μ	p	C	σ/μ
2	0	1.0000 ± 0.0001 [1]	-12.38 -58.15	1.73×10^{-4}	1.0000 ± 0.0001 [1]	-6.15 -29.08	1.97×10^{-4}
2	1	1.0003 ± 0.0009 [1]	11.36 -56.10	2.27×10^{-3}	1.0000 ± 0.0001 [1]	5.63 -27.83	1.79×10^{-3}
2	2	1.0001 ± 0.0003 [1]	78.47 -50.92	9.23×10^{-3}	0.9998 ± 0.0006 [1]	38.56 -25.92	6.10×10^{-3}
2	3	0.9963 ± 0.0122 [1]	211.66 -48.07	1.82×10^{-2}	0.9976 ± 0.0080 [1]	108.75 -26.40	1.20×10^{-2}
3	0	0.9998 ± 0.0006 [1]	-14.19 -51.56	9.37×10^{-4}	1.0000 ± 0.0001 [1]	-7.07 -25.93	1.91×10^{-4}
3	1	1.0005 ± 0.0017 [1]	-8.10 -54.22	2.46×10^{-3}	1.0002 ± 0.0008 [1]	-3.94 -26.93	1.25×10^{-3}
3	2	1.0007 ± 0.0023 [1]	9.42 -57.91	5.36×10^{-3}	1.0002 ± 0.0005 [1]	4.54 -28.58	3.49×10^{-3}
3	3	1.0006 ± 0.0019 [1]	47.62 -60.43	1.48×10^{-2}	1.0001 ± 0.0002 [1]	22.74 -30.42	9.53×10^{-3}
4	0	0.9997 ± 0.0012 [1]	-14.48 -49.70	1.70×10^{-3}	1.0000 ± 0.0000 [1]	-7.23 -25.08	1.78×10^{-5}
4	1	1.0003 ± 0.0009 [1]	-11.66 -51.66	1.36×10^{-3}	1.0002 ± 0.0007 [1]	-5.72 -25.81	1.01×10^{-3}
4	2	1.0009 ± 0.0029 [1]	-4.16 -54.94	4.29×10^{-3}	1.0004 ± 0.0012 [1]	-1.98 -27.13	2.15×10^{-3}
4	3	1.0009 ± 0.0030 [1]	11.53 -58.38	7.46×10^{-3}	1.0003 ± 0.0008 [1]	5.47 -28.76	4.80×10^{-3}

b. Higher-order contamination in the numerical extraction. Although the underlying field equations are linearized in ζ , the numerical procedure used to extract $\omega(\zeta)$ via Leaver’s method can effectively introduce higher-order dependence on ζ . Two immediate sources are: (i) the Gaussian-elimination band-reduction step, which combines ζ -dependent terms and therefore generates products that promote higher powers of ζ ⁴, and (ii) the nonlinear Newton solver employed to locate the roots of the continued fraction, which can also imprint nonlinear ζ -dependence through its iterative updates. As a result, the numerically extracted frequency is more accurately viewed as an expansion

$$\Delta\omega(\zeta) \equiv \omega(\zeta) - \omega(0) = a_1 \zeta + a_2^{(1)} \zeta^2 + a_3^{(1)} \zeta^3 + \dots,$$

⁴ A strictly linear-in- ζ reduction can be enforced by truncating to $\mathcal{O}(\zeta)$ after each elimination step, nevertheless, we do not impose this truncation in our implementation.

⁵ where a_1 is the linear coefficient, while $a_2^{(1)}, a_3^{(1)}, \dots$ denote effective higher-order contributions induced by the Leaver extraction procedure, even when the input perturbation is truncated at $\mathcal{O}(\zeta)$. Consequently, estimating a_1 —especially in cases where the linear contribution is suppressed or vanishes for a given operator—is a subtle task.

c. Diagnostics. Hence, to characterize the ζ -dependence of $\omega(\zeta)$ for both the null and control operators, we employ the following diagnostics:

- **Leading-power diagnostic:** determine the dominant scaling $\Delta\omega(\zeta) \propto \zeta^p$ in the different- ζ regime.
- **Polynomial fitting:** fit the shift $\Delta\omega(\zeta)$ with a polynomial in ζ to extract the linear coefficient and quantify higher-order contamination.

⁵ Here in this subsection, we re-use $\omega(\zeta)$ to denote the Leaver extracted frequency.

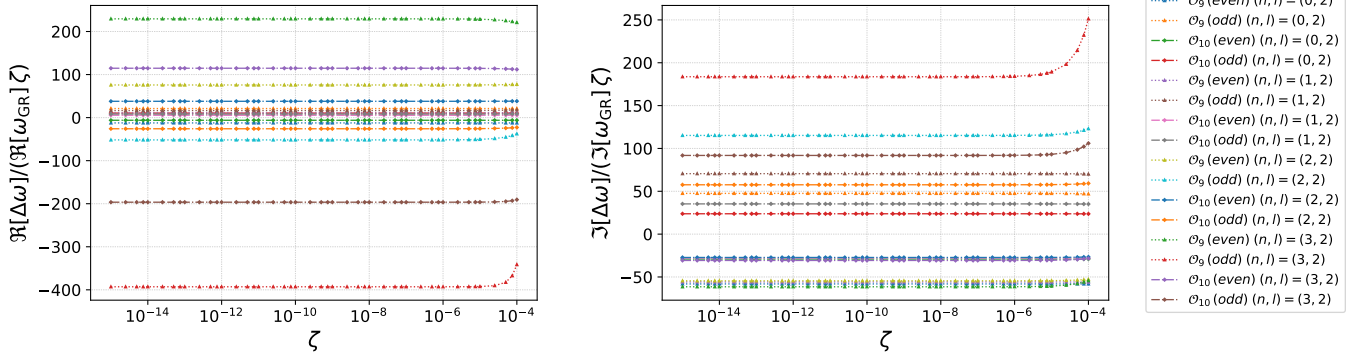


FIG. 4. Scaling test of the EFT frequency shift for \mathcal{O}_9 and \mathcal{O}_{10} at $\ell = 2$. The left (right) panel shows $\Re(\delta_{\text{Leaver}}/\zeta)$ ($\Im(\delta_{\text{Leaver}}/\zeta)$) versus the coupling ζ . The near-flat behavior supports a leading linear dependence on ζ , while departures at the largest ζ indicate the onset of higher-order contamination.

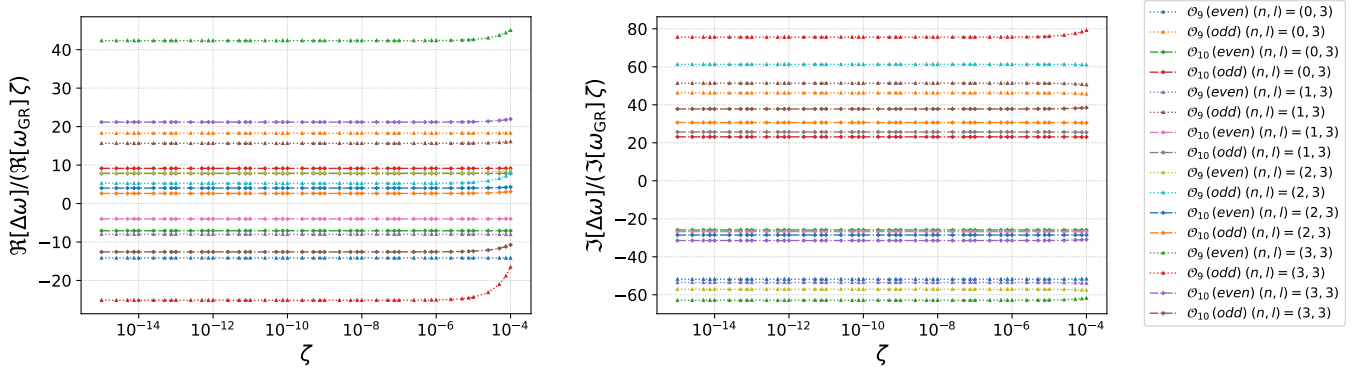


FIG. 5. Same as Fig. 4, but for $\ell = 3$.

1. What is the leading power?

We model the deviation as a power law in the coupling range set by a chosen cutoff ζ_{max} ,

$$\delta_{\text{Leaver}}(\zeta) \equiv \left(\frac{\Re(\Delta\omega(\zeta))}{\Re(\omega(0))}, \frac{\Im(\Delta\omega(\zeta))}{\Im(\omega(0))} \right) \approx C \zeta^p, \quad (48)$$

where the coefficient $C \in \mathbb{C}$ are generally complex.

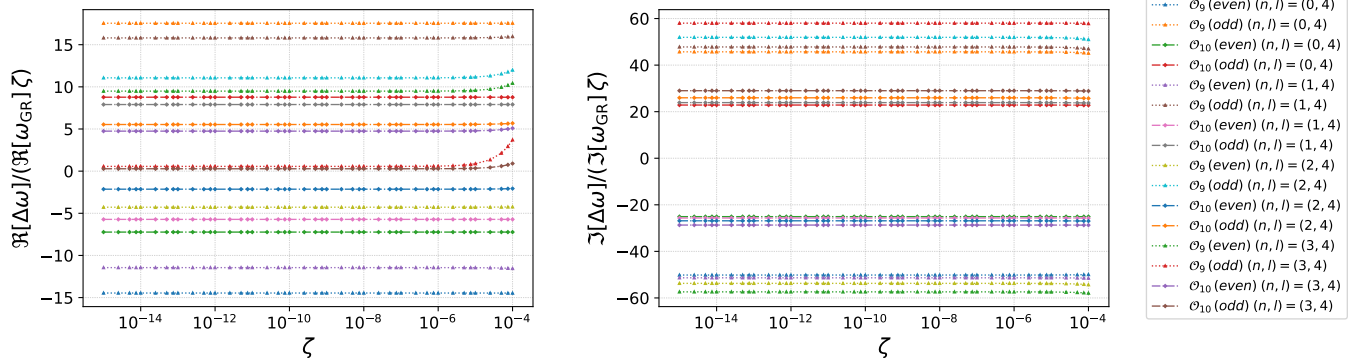
On a chosen coupling window $[\zeta_{\text{min}}, \zeta_{\text{max}}]$, we then infer the leading scaling via two complementary steps: (i) estimate a continuous effective exponent p_{eff} from log-log slopes of the amplitude $\|\delta_{\text{Leaver}}\|$ across adjacent ζ values, and we then average these local slope estimates across the ζ points within the chosen fitting window $[\zeta_{\text{min}}, \zeta_{\text{max}}]$ to obtain the reported p_{eff} (with scatter across the window used to define σ_p), and (ii) test candidate integers $p \in \{1, 2, 3\}$ by rescaling the data by ζ^p and selecting the p_* that makes the rescaled complex series as flat as possible. Finally, with p_* fixed, we obtain the corresponding complex coefficient C from a least-squares fit using the flatness ratio σ/μ reported in the tables where N , μ and σ is the sample population, mean and standard deviation respectively inside the fit window.

a. Null operators. Figures 1–3 show scaled δ_{Leaver} across our ζ sampling and visually indicate a leading quadratic behaviour for the null combinations. To quantify the leading power, we apply the windowed diagnostics described above, using data restricted to $\zeta \leq \zeta_{\text{max}}$.

At the widest diagnostic window $\zeta_{\text{max}} = 10^{-3}$ (Tables IV and V), the null-sector data select $p_* = 2$ for both \mathcal{O}_5 and \mathcal{O}_8 across all listed modes and both parities. The effective exponents are tightly clustered around 2: for \mathcal{O}_5 and \mathcal{O}_8 , $|p_{\text{eff}} - 2| \lesssim 10^{-3}$ and $\lesssim 10^{-4}$ respectively. The complex flatness ratios are small and mode-dependent: $\sigma/\mu \simeq 10^{-4} - 10^{-3}$ for \mathcal{O}_5 and \mathcal{O}_8 . Together, these diagnostics support a leading quadratic scaling for both null operators in both parities.

Upon tightening the window to $\zeta_{\text{max}} = 10^{-4}$ and 10^{-5} (as shown in Tables XXI, XXII, XXIII, and XXIV), the same $p_* = 2$ conclusion is reinforced: p_{eff} moves closer to 2 and σ/μ decreases, consistent with convergence toward the asymptotic quadratic regime. We therefore identify $p = 2$ as the leading power for both null operators in both parities.

b. Control operators. Figures 4–6 display scaled δ_{Leaver} over the full sampled ζ range and visually support a leading linear scaling for the control operators.

FIG. 6. Same as Fig. 4, but for $\ell = 4$.

As above, we quantify the leading power using the windowed diagnostics on data restricted to $\zeta \leq \zeta_{\max}$.

At the widest diagnostic window $\zeta_{\max} = 10^{-3}$ (Tables VI and VII), both \mathcal{O}_9 and \mathcal{O}_{10} select $p_{\star} = 1$ for every listed mode and both parities. For \mathcal{O}_9 and \mathcal{O}_{10} , the effective exponents remain close to unity, with $|p_{\text{eff}} - 1| \lesssim 10^{-3}$ and $\lesssim 10^{-3}$ respectively. Yet, there are some higher-overtone outliers (down to $p_{\text{eff}} = 0.9963$ in even parity and $p_{\text{eff}} = 0.9896$ in odd parity). This non-asymptotic contamination is mirrored in the complex flatness: in odd parity, $\sigma/\mu \simeq 10^{-3}$ – 10^{-1} for \mathcal{O}_9 and $\sigma/\mu \simeq 10^{-3}$ – 10^{-2} for \mathcal{O}_{10} , with the largest scatter occurring at the highest listed overtone. It's also evident that even parity is systematically cleaner.

Tightening the window to $\zeta_{\max} = 10^{-4}$ and 10^{-5} (as shown in Tables XVII, XVIII, XIX, and XX) preserves the same $p_{\star} = 1$ selection while reducing uncertainties and significantly decreasing σ/μ ; the fitted complex coefficient C (reported via $\Re(C) | \Im(C)$) varies only mildly across windows, consistent with a well-resolved linear leading term.

2. Polynomial fits

Our primary goal is to test whether the null operators produce a genuinely linear-in- ζ correction to the vacuum QNM spectrum. In practice, as discussed above, the Leaver-type numerical implementation introduces a mild nonlinear dependence in ζ . Having already determined the leading power of ζ for all operators considered in this work, we now investigate the subleading structure by fitting the frequency shift $\Delta\omega(\zeta)$ with a polynomial in ζ ,

$$\delta_{\text{Leaver}}(\zeta) \approx \sum_{k=1}^K c_k^{(b)} \zeta^k,$$

where the complex coefficients $c_k^{(b)}$ are obtained from least-squares fits over suitably chosen windows.

First, since higher-order terms become influential when the fit extends to relatively large values of ζ , we re-

strict attention to a sweet-spot region that is well below our largest deformation, $\zeta = 10^{-3}$, but still contains enough data points to make all diagnostics meaningful. We choose to work with ten nested fitting windows whose upper endpoints are

$$\zeta_{\max} \in \{2.5 \times 10^{-11}, 5 \times 10^{-11}, 7.5 \times 10^{-11}, 10^{-10}, 2.5 \times 10^{-10}, 5 \times 10^{-10}, 7.5 \times 10^{-10}, 10^{-9}, 2.5 \times 10^{-9}, 5 \times 10^{-9}\}. \quad (49)$$

Second, we deliberately restrict attention to three nested models M_b with $b \in \{1, 12, 123\}$:

$$\begin{aligned} M_1 : \quad \Delta\omega(\zeta) &\approx c_1^{(1)} \zeta, \\ M_{12} : \quad \Delta\omega(\zeta) &\approx c_1^{(12)} \zeta + c_2^{(12)} \zeta^2, \\ M_{123} : \quad \Delta\omega(\zeta) &\approx c_1^{(123)} \zeta + c_2^{(123)} \zeta^2 + c_3^{(123)} \zeta^3, \end{aligned}$$

where we use M_{123} only for the null-operator cases.

Moreover, although our calculated QNMs have ~ 60 digits of precision and we could in principle include work with M_{1234} as well, we won't to avoid overfitting⁶. This is the same reason why M_{123} is not going to be used for control cases.

As we will show below for null operators, the fitted values of $c_1^{(12),(123)}$ is expected to be much smaller than the actual values. In other words, stopping at ζ^3 term is conservative and the linear coefficient $c_1^{(123)}$ can be interpreted as a lower bound on any true linear-in- ζ contribution.

Third, to decide which model to adopt and which coefficients to trust, we use two simple but strict criteria. For each model M_b and coefficient index k , we denote by $c_{k,i}^{(b)}$ the value obtained in the i -th ζ_{\max} window and by

⁶ Nevertheless, when stated explicitly, we also fit M_{1234} as a reference model; it is not used to set our reported bounds or conclusions.

$\bar{c}_k^{(b)}$ their mean. We then define the stability measure

$$\Gamma_k^{(b)} \equiv \frac{\max_i |c_{k,i}^{(b)} - \bar{c}_k^{(b)}|}{|\bar{c}_k^{(b)}|} < 10^{-4}.$$

In practice, for null operators, $c_2^{(b)}$ and $c_3^{(b)}$ satisfy this criterion by many orders of magnitude, while $c_1^{(b)}$ typically does not, as expected. However, for control cases it will.

By progressively building up the polynomial models M_1 , M_{12} , and M_{123} , we monitor both the coefficient stability and the root-mean-square (RMS) residual of the fit as the polynomial degree increases. We select the lowest-order model whose coefficients pass the stability criterion and for which the RMS error has already saturated.

a. Null operators. For the null-operator cases the polynomial fits exhibit a clear hierarchy. As we enlarge the model from M_1 to M_{12} the RMS residual decrease by roughly 10^{-10} , and it decrease by a further $\sim 10^{-10}$ upon moving to M_{123} . Extending once more to M_{1234} causes yet another $\sim 10^{-1} - 10^{-2}$ decrease, indicate a saturation in the fitting. At the same time, the additional parameters beyond cubic order fail our coefficient-stability requirement, indicating that these higher-degree models c_1 and $c_{>3}$ will start canceling each other.

A useful way to interpret this behavior is to inspect the relative contributions of the fitted terms to $\Delta\omega(\zeta)$ over the fitting window. In the null cases, the quadratic term dominates overwhelmingly: in the degree-3 model, $c_2^{(123)}\zeta^2$ accounts for $\simeq 1 - \mathcal{O}(10^{-7})$ of the reconstructed shift, whereas the linear and cubic pieces contribute only at the level of $\sim 10^{-14}\%$ and $\sim 10^{-5}\%$, respectively. This extreme suppression implies a large budget for still-higher powers. For example, in M_{1234} , a quartic contribution of order $10^{-11}\%$ will knock $\text{median}(|c_1^{1234}|)$ by 10^{-3} yet it stable only among fewer number of windows and it doesn't. Consequently, the fitted $c_1^{(123)}$ should be

viewed as a conservative *upper bound* rather than a measurement: we expect the true linear coefficient to satisfy $|c_1| \ll |c_1^{(123)}|$.

In practice, M_{123} emerges as the best compromise: it is the highest-order model whose coefficients remain stable across the nested ζ_{\max} windows, while simultaneously yielding the lowest RMS residual among the stable models. Quantitatively, across all modes in Tables VIII, IX, and X we find

$$\begin{aligned} \min(|c_1^{(123)}|) &= 3.09 \times 10^{-24}, \\ \text{median}(|c_1^{(123)}|) &= 5.15 \times 10^{-22}, \\ \max(|c_1^{(123)}|) &= 4.60 \times 10^{-20}, \end{aligned} \quad (50)$$

b. Control operators. In the control data, the change $\Delta\omega(\zeta)$ is dominated by the linear term. In the M_{12} fits, this is borne out quantitatively by the contribution audit: $|c_1^{(12)}\zeta|$ accounts for $1 - \mathcal{O}(10^{-7})$ of the reconstructed shift over the fitting window, while the quadratic correction remains suppressed at the level $|c_2^{(12)}\zeta^2| \sim 10^{-8} - 10^{-5}$. Consistently, $c_1^{(12)}$ is extremely stable across nested ζ_{\max} windows at the ~ 11 - 14 ($10^{-11}\%$) digit level, whereas $c_2^{(12)}$ is stable at only ~ 5 - 6 digits ($10^{-4}\%$). See Tables XI, XII and XIII for further details.

Furthermore, across all ratios between QNMs shift due to \mathcal{O}_9 to \mathcal{O}_{10} are extremely close to 2 with the largest absolute deviation is $\max|\mathcal{R}_{9/10} - 2| \sim 10^{-11}$. As was the case for EVP case, the deviation increases with higher overtone.

We verified that the QNM frequencies for the physical operators extracted with the Leaver method are consistent with Ref. [1]: when rounded to the two decimal places reported in their Table I, our values coincide with theirs.

C. Cross Check: EVP Vs Leaver

We quantify agreement between the EVP results and the Leaver Model M_{12} fit coefficient $c_1^{(12)}$, by using the symmetric relative difference

$$\epsilon_X \equiv \frac{2||\delta_{\text{EVP } X} - \delta_{\text{Leaver } X}||}{|\delta_{\text{EVP } X}| + |\delta_{\text{Leaver } X}|}, \quad X \in \{\Re, \Im\}, \quad (51)$$

computed mode-by-mode for $\ell = 2, 3, 4$, $n = 0, 1, 2, 3$, both operators $\mathcal{O}_9, \mathcal{O}_{10}$, and both parities. Aggregating all comparisons, we find

$$\begin{aligned} \min(\epsilon_{\Re}, \epsilon_{\Im}) &= (3.54 \times 10^{-17}, 3.54 \times 10^{-16}), \\ \text{median}(\epsilon_{\Re}, \epsilon_{\Im}) &= (9.48 \times 10^{-14}, 2.66 \times 10^{-14}), \\ \max(\epsilon_{\Re}, \epsilon_{\Im}) &= (1.13 \times 10^{-6}, 1.59 \times 10^{-7}). \end{aligned} \quad (52)$$

Overall most of those discrepancies (but not all) are closely aligned with the numerical floor we estimated for the null operators QNMs using the EVP. This might suggest that the Leaver M_{12} coefficient $c_1^{(12)}$ reproduces the EVP results to near the numerical floor set by the EVP extraction.

Two systematic trends mirror those seen in the EVP null-operator analysis: at fixed ℓ the disagreement typically increases with overtone n , while at fixed n it decreases with increasing ℓ . The largest mismatch occurs at $(\ell, n) = (2, 3)$, whereas higher- ℓ fundamentals show the tightest agreement. See Tables IV B 2 b-IV B 2 b.

TABLE VIII. Coefficient stability summary for degree 3 ($\Delta\omega(\zeta) = \sum_{k=1}^3 c_k \zeta^k$), with real and imaginary parts for each mode.

	c_k	(0, 2)		(1, 2)		(2, 2)		(3, 2)	
		\Re	\Im	\Re	\Im	\Re	\Im	\Re	\Im
\mathcal{O}_5	$o c_1$	3.7×10^{-22}	-7.6×10^{-22}	2.7×10^{-21}	1.7×10^{-21}	6.6×10^{-21}	1.1×10^{-20}	-2.4×10^{-20}	3.9×10^{-20}
	$o c_2$	119.9	477.1	-35.73	596.0	-687.3	736.9	-2796.0	921.4
	$o c_3$	7831.0	1.065×10^4	1.656×10^4	3.98×10^4	-1.409×10^4	9.63×10^4	-3.062×10^5	1.96×10^5
	$e c_1$	4.1×10^{-22}	-8.0×10^{-22}	2.7×10^{-21}	1.9×10^{-21}	5.0×10^{-21}	1.1×10^{-20}	-3.1×10^{-20}	3.4×10^{-20}
	$e c_2$	124.5	497.3	-43.28	599.0	-711.0	712.8	-2783.0	833.7
	$e c_3$	8379.0	1.107×10^4	1.636×10^4	4.212×10^4	-2.386×10^4	9.494×10^4	-3.246×10^5	1.712×10^5
\mathcal{O}_8	$o c_1$	1.5×10^{-24}	-2.7×10^{-24}	1.1×10^{-23}	6.8×10^{-24}	2.5×10^{-23}	4.4×10^{-23}	-9.4×10^{-23}	1.5×10^{-22}
	$o c_2$	7.491	29.82	-2.233	37.25	-42.95	46.06	-174.8	57.58
	$o c_3$	122.4	166.5	258.8	621.9	-220.1	1505.0	-4784.0	3062.0
	$e c_1$	1.7×10^{-24}	-2.9×10^{-24}	1.1×10^{-23}	7.9×10^{-24}	1.9×10^{-23}	4.4×10^{-23}	-1.2×10^{-22}	1.4×10^{-22}
	$e c_2$	7.782	31.08	-2.705	37.44	-44.44	44.55	-173.9	52.11
	$e c_3$	130.9	173.0	255.6	658.1	-372.8	1483.0	-5072.0	2676.0

TABLE IX. Coefficient stability summary for degree 3 ($\Delta\omega(\zeta) = \sum_{k=1}^3 c_k \zeta^k$), with real and imaginary parts for each mode.

	c_k	(0, 3)		(1, 3)		(2, 3)		(3, 3)	
		\Re	\Im	\Re	\Im	\Re	\Im	\Re	\Im
\mathcal{O}_5	$o c_1$	8.5×10^{-23}	-2.0×10^{-21}	1.4×10^{-21}	-2.3×10^{-21}	7.5×10^{-21}	-2.4×10^{-22}	2.5×10^{-20}	1.1×10^{-20}
	$o c_2$	156.6	482.6	136.1	598.6	26.16	757.2	-332.0	979.1
	$o c_3$	7007.0	-6011.0	2.056×10^4	1.296×10^4	4.698×10^4	5.185×10^4	7.319×10^4	1.276×10^5
	$e c_1$	9.0×10^{-23}	-2.1×10^{-21}	1.5×10^{-21}	-2.2×10^{-21}	7.6×10^{-21}	-5.1×10^{-24}	2.4×10^{-20}	1.1×10^{-20}
	$e c_2$	158.3	488.6	136.2	603.3	21.27	759.9	-348.5	973.8
	$e c_3$	7134.0	-6324.0	2.094×10^4	1.356×10^4	4.654×10^4	5.346×10^4	6.819×10^4	1.285×10^5
\mathcal{O}_8	$o c_1$	4.1×10^{-25}	-7.7×10^{-24}	5.6×10^{-24}	-8.5×10^{-24}	2.9×10^{-23}	-5.8×10^{-25}	9.8×10^{-23}	4.3×10^{-23}
	$o c_2$	9.79	30.16	8.507	37.41	1.635	47.33	-20.75	61.2
	$o c_3$	109.5	-93.92	321.3	202.4	734.1	810.1	1144.0	1994.0
	$e c_1$	4.3×10^{-25}	-7.9×10^{-24}	5.8×10^{-24}	-8.5×10^{-24}	3.0×10^{-23}	3.5×10^{-25}	9.5×10^{-23}	4.5×10^{-23}
	$e c_2$	9.893	30.54	8.514	37.71	1.329	47.49	-21.78	60.86
	$e c_3$	111.5	-98.81	327.2	211.9	727.3	835.4	1066.0	2008.0

V. DISCUSSION AND CONCLUSION

Next-generation gravitational-wave observatories will enable high-SNR ringdown measurements and make black-hole QNMs increasingly sensitive probes of small, high-scale deviations from GR in the dynamical strong-field regime [2, 4, 6, 40]. A controlled way to parameterize such deviations is the gravitational EFT, in which new physics is encoded in higher-curvature operators suppressed by a high scale [1]. Before interpreting tiny EFT-induced QNM shifts as physical predictions, however, the framework and its numerical extraction must be stress-tested: (i) the problem is intrinsically two-parameter, involving both the GW perturbation order ϵ and the EFT deformation ζ ; and (ii) the expected signals can be comparable to the numerical floor, especially for overtones, unless precision and convergence are tightly controlled.

We therefore designed two null tests. First, we compute the QNM response to operators \mathcal{O}_5 and \mathcal{O}_8 , which

must not generate any first-order ($\mathcal{O}(\zeta)$) shift at vacuum; any sufficiently significant nonzero result directly diagnoses a breakdown of the scheme. Second, exploiting the Ricci-flat identity that ties \mathcal{O}_9 to \mathcal{O}_{10} (up to linear and higher Ricci terms), we check numerically that—when the Wilson coefficients are set equal—the ratio between the extracted QNM shifts should be 2.

We use two independent and complementary QNM strategies. First, we implement the EVP method to extract the linear frequency correction ω_1 from a bilinear form evaluated along a complex contour, with the GR RW/Zerilli sector reconstructed at high precision. Second, we built a generalized Leaver approach that solves the EFT master equation directly: we derive the banded Frobenius recurrences, perform an exact band reduction to a three-term system, and apply a scalar continued-fraction solver.

It is worth emphasizing that the two approaches are complementary. EVP has two practical advantages: (i)

TABLE X. Coefficient stability summary for degree 3 ($\Delta\omega(\zeta) = \sum_{k=1}^3 c_k \zeta^k$), with real and imaginary parts for each mode.

	c_k	(0, 4)		(1, 4)		(2, 4)		(3, 4)	
		\Re	\Im	\Re	\Im	\Re	\Im	\Re	\Im
\mathcal{O}_5	${}^o c_1$	-4.9×10^{-23}	-2.0×10^{-21}	3.5×10^{-22}	-3.1×10^{-21}	2.9×10^{-21}	-4.5×10^{-21}	1.2×10^{-20}	-3.8×10^{-21}
	${}^o c_2$	165.8	463.5	168.7	556.6	151.8	677.7	67.34	850.5
	${}^o c_3$	5699.0	-1.424×10^4	1.492×10^4	-3752.0	3.647×10^4	1.584×10^4	7.512×10^4	5.643×10^4
	${}^e c_1$	-5.0×10^{-23}	-2.1×10^{-21}	3.6×10^{-22}	-3.1×10^{-21}	3.0×10^{-21}	-4.5×10^{-21}	1.3×10^{-20}	-3.6×10^{-21}
	${}^e c_2$	166.5	465.5	169.2	558.6	151.4	680.0	64.25	852.2
	${}^e c_3$	5731.0	-1.449×10^4	1.507×10^4	-3719.0	3.668×10^4	1.637×10^4	7.48×10^4	5.746×10^4
\mathcal{O}_8	${}^o c_1$	-1.1×10^{-25}	-7.7×10^{-24}	1.4×10^{-24}	-1.2×10^{-23}	1.2×10^{-23}	-1.7×10^{-23}	4.9×10^{-23}	-1.4×10^{-23}
	${}^o c_2$	10.36	28.97	10.54	34.79	9.485	42.35	4.209	53.15
	${}^o c_3$	89.05	-222.5	233.1	-58.63	569.9	247.5	1174.0	881.7
	${}^e c_1$	-1.1×10^{-25}	-7.8×10^{-24}	1.5×10^{-24}	-1.2×10^{-23}	1.2×10^{-23}	-1.7×10^{-23}	4.9×10^{-23}	-1.4×10^{-23}
	${}^e c_2$	10.4	29.09	10.57	34.91	9.46	42.5	4.015	53.26
	${}^e c_3$	89.55	-226.5	235.5	-58.1	573.1	255.7	1169.0	897.8

TABLE XI. Coefficient stability summary for degree 2 ($\Delta\omega(\zeta) = \sum_{k=1}^3 c_k \zeta^k$), with real and imaginary parts for each mode.

	c_k	(0, 2)		(1, 2)		(2, 2)		(3, 2)	
		\Re	\Im	\Re	\Im	\Re	\Im	\Re	\Im
\mathcal{O}_9	${}^o c_1$	21.072	47.529	16.362	70.574	-51.795	115.18	-392.92	183.67
	${}^o c_2$	878.35	-5724.0	19342.0	-3665.4	1.2052×10^5	82766.0	25356.0	5.4812×10^5
	${}^e c_1$	-12.339	-58.117	10.758	-55.815	75.805	-54.477	229.39	-61.441
	${}^e c_2$	-192.46	-154.32	2869.2	-1587.4	15666.0	17652.0	-83385.0	79190.0
\mathcal{O}_{10}	${}^o c_1$	10.536	23.764	8.1809	35.287	-25.897	57.589	-196.46	91.834
	${}^o c_2$	-17.661	-1072.4	3693.3	-1852.9	28896.0	16718.0	16490.0	1.2713×10^5
	${}^e c_1$	-6.1697	-29.059	5.3792	-27.908	37.902	-27.238	114.7	-30.72
	${}^e c_2$	89.514	-114.32	1227.5	315.55	3680.5	6463.4	-28099.0	23393.0

it targets the linear response by construction, extracting ω_1 directly with no fitting needed to separate $\mathcal{O}(\zeta)$ from higher-order terms; and (ii) once the analytic structure is fixed (branch cuts and contour choice), it is relatively straightforward to implement numerically. By contrast, the generalized Leaver method is intentionally blind to the perturbative bookkeeping—it simply solves the EFT master equation at finite ζ —and this is precisely its strength: it enables direct scans in ζ and provides a clean diagnostic for when higher-order contamination sets in, i.e., when $\omega(\zeta)$ departs from $\omega_0 + \zeta\omega_1 + \zeta^2\omega_2 + \mathcal{O}(\zeta^3)$.

a. Null Tests: (i) Null Operators . On a Ricci-flat background, the operators \mathcal{O}_5 and \mathcal{O}_8 are removable by local field redefinitions and therefore induce no first-order ($\mathcal{O}(\zeta)$) vacuum QNM shifts in theory [1, 7]. This provides a sharp, operator-level null prediction against which both solvers can be stress-tested.

Using EVP across multipoles $\ell = 2, 3, 4$ and overtones $n = 0, 1, 2, 3$, we find that the extracted first-order fractional shifts in the null sector are consistent with zero down to a mode-dependent numerical floor. Aggregating over the full (n, ℓ) grid yields $|\delta_{\text{EVP, min}}| \sim 10^{-28}$, $|\delta_{\text{EVP, median}}| \sim 10^{-18}$, and $|\delta_{\text{EVP, max}}| \lesssim 10^{-8}$, with the

largest residuals occurring at low ℓ and high n , consistent with the increased numerical sensitivity of overtone extraction.

Independently, in the Leaver approach we confirm that, in the null sector, the dominant dependence of $\Delta\omega(\zeta)$ is quadratic (i.e., $\propto \zeta^2$). Moreover, fitting $\Delta\omega(\zeta)$ with polynomial models under harsh requirement shows that the cubic model M_{123} is the most stable (lowest RMS and flattest fit coefficients $\{c_2^{(123)}, c_3^{(123)}\}$ across 11 different fitting windows) for the null-operator diagnostics. Scanning in ζ confirms that any apparent linear correction $c_1^{(123)}$ at $\mathcal{O}(\zeta)$ is strongly suppressed and consistent with numerical noise, with representative floors $|\delta_{\text{Leaver, min}}| \lesssim 10^{-24}$, $|\delta_{\text{Leaver, median}}| \lesssim 10^{-22}$, and $|\delta_{\text{Leaver, max}}| \lesssim 10^{-20}$. This makes Leaver estimates for the numerical floor is much more tighter, at same level of EVP diagnostics.

Focusing on the fundamental modes ($n = 0$) and taking the magnitude of the complex shifts over $\ell = 2, 3, 4$ using EVP (Tables I–III), we obtain $|\delta_{\text{EVP}}^{n=0}|_{\text{min, med, max}} \lesssim (10^{-26}, 10^{-23}, 10^{-17})$. While the corresponding linear coefficient in the M_{123} fit, the $n = 0$ results in Tables VIII–X imply

TABLE XII. Coefficient stability summary for degree 2 ($\Delta\omega(\zeta) = \sum_{k=1}^3 c_k \zeta^k$), with real and imaginary parts for each mode.

	c_k	(0, 3)		(1, 3)		(2, 3)		(3, 3)	
		\Re	\Im	\Re	\Im	\Re	\Im	\Re	\Im
\mathcal{O}_9	${}_o c_1$	18.289	46.265	15.647	51.392	5.2511	61.309	-25.138	75.63
	${}_o c_2$	329.92	-5880.2	4520.4	-8128.7	25401.0	-679.63	78221.0	40799.0
	${}_e c_1$	-14.149	-51.817	-7.9918	-53.533	8.0346	-57.094	42.345	-62.886
	${}_e c_2$	-196.85	1219.1	-588.48	-3160.8	6344.8	-4489.1	28293.0	9939.7
\mathcal{O}_{10}	${}_o c_1$	9.1445	23.133	7.8237	25.696	2.6255	30.655	-12.569	37.815
	${}_o c_2$	-63.314	-923.07	515.92	-2050.3	4965.9	-1378.1	17745.0	7043.9
	${}_e c_1$	-7.0743	-25.908	-3.9959	-26.767	4.0173	-28.547	21.172	-31.443
	${}_e c_2$	16.534	-122.15	249.11	-804.15	2487.2	-291.16	8141.7	4624.4

TABLE XIII. Coefficient stability summary for degree 2 ($\Delta\omega(\zeta) = \sum_{k=1}^3 c_k \zeta^k$), with real and imaginary parts for each mode.

	c_k	(0, 4)		(1, 4)		(2, 4)		(3, 4)	
		\Re	\Im	\Re	\Im	\Re	\Im	\Re	\Im
\mathcal{O}_9	${}_o c_1$	17.545	45.703	15.804	47.798	11.067	51.928	0.5627	58.02
	${}_o c_2$	124.05	-5784.2	1733.0	-8123.4	9596.9	-8663.7	31503.0	693.51
	${}_e c_1$	-14.46	-50.165	-11.445	-51.351	-4.2793	-53.74	9.492	-57.393
	${}_e c_2$	-84.342	2147.0	-1001.1	-1338.9	320.76	-5643.1	9165.3	-5740.8
\mathcal{O}_{10}	${}_o c_1$	8.7725	22.852	7.9022	23.899	5.5334	25.964	0.28135	29.01
	${}_o c_2$	-77.687	-814.44	42.925	-1710.9	1472.9	-2497.3	6268.1	-1214.2
	${}_e c_1$	-7.23	-25.082	-5.7226	-25.676	-2.1397	-26.87	4.746	-28.697
	${}_e c_2$	11.424	1.0423	-9.5121	-646.49	716.05	-1247.6	3427.0	-504.68

		(0, 2)	(1, 2)	(2, 2)	(3, 2)
\mathcal{O}_9	even	$3.12 \times 10^{-16}, 1.11 \times 10^{-15}$	$1.2 \times 10^{-13}, 4.08 \times 10^{-14}$	$2.91 \times 10^{-10}, 2.43 \times 10^{-11}$	$1.13 \times 10^{-6}, 1.59 \times 10^{-7}$
	odd	$1.25 \times 10^{-14}, 5.72 \times 10^{-15}$	$1.06 \times 10^{-13}, 1.19 \times 10^{-13}$	$4.29 \times 10^{-10}, 2.5 \times 10^{-11}$	$7.28 \times 10^{-7}, 5.31 \times 10^{-8}$
\mathcal{O}_{10}	even	$9.59 \times 10^{-16}, 3.54 \times 10^{-16}$	$1.38 \times 10^{-13}, 5.16 \times 10^{-14}$	$2.91 \times 10^{-10}, 2.48 \times 10^{-11}$	$1.13 \times 10^{-6}, 1.59 \times 10^{-7}$
	odd	$1.65 \times 10^{-15}, 1.35 \times 10^{-15}$	$7.35 \times 10^{-14}, 1.58 \times 10^{-14}$	$4.32 \times 10^{-10}, 2.5 \times 10^{-11}$	$7.28 \times 10^{-7}, 5.31 \times 10^{-8}$

TABLE XIV. Symmetric relative errors between EVP and Leaver degree-2 fit using c_1 values for $\ell = 2$, computed component-wise ϵ_X . Each cell lists $\epsilon_{\Re}, \epsilon_{\Im}$.

		(0, 3)	(1, 3)	(2, 3)	(3, 3)
\mathcal{O}_9	even	$2.08 \times 10^{-15}, 8.52 \times 10^{-16}$	$3.26 \times 10^{-14}, 8.16 \times 10^{-15}$	$1.6 \times 10^{-13}, 4.93 \times 10^{-14}$	$3.51 \times 10^{-13}, 1.64 \times 10^{-13}$
	odd	$8.28 \times 10^{-15}, 6.9 \times 10^{-15}$	$1.08 \times 10^{-13}, 4.57 \times 10^{-14}$	$1.98 \times 10^{-13}, 3.07 \times 10^{-13}$	$3.69 \times 10^{-12}, 5.87 \times 10^{-13}$
\mathcal{O}_{10}	even	$1.14 \times 10^{-16}, 6.84 \times 10^{-16}$	$1.5 \times 10^{-14}, 1.13 \times 10^{-15}$	$9.08 \times 10^{-17}, 2.2 \times 10^{-14}$	$1.59 \times 10^{-13}, 4.24 \times 10^{-14}$
	odd	$4.18 \times 10^{-16}, 2.52 \times 10^{-15}$	$2.25 \times 10^{-14}, 1.01 \times 10^{-15}$	$1.31 \times 10^{-13}, 5.5 \times 10^{-14}$	$6.24 \times 10^{-13}, 1.41 \times 10^{-13}$

TABLE XV. Same Layout as in XI but for $\ell = 3$.

		(0, 4)	(1, 4)	(2, 4)	(3, 4)
\mathcal{O}_9	even	$1.44 \times 10^{-15}, 4.94 \times 10^{-15}$	$3.81 \times 10^{-15}, 1.12 \times 10^{-14}$	$2.41 \times 10^{-13}, 7.42 \times 10^{-15}$	$2.76 \times 10^{-13}, 7.52 \times 10^{-14}$
	odd	$4.82 \times 10^{-15}, 1.46 \times 10^{-14}$	$6.49 \times 10^{-14}, 2.06 \times 10^{-15}$	$3.47 \times 10^{-13}, 1.3 \times 10^{-13}$	$3.23 \times 10^{-12}, 4.75 \times 10^{-13}$
\mathcal{O}_{10}	even	$1.81 \times 10^{-16}, 5.06 \times 10^{-16}$	$4.38 \times 10^{-15}, 2.29 \times 10^{-15}$	$8.08 \times 10^{-14}, 4.8 \times 10^{-15}$	$1.76 \times 10^{-14}, 3.13 \times 10^{-14}$
	odd	$3.54 \times 10^{-17}, 2.39 \times 10^{-15}$	$8.98 \times 10^{-15}, 6.25 \times 10^{-15}$	$8.31 \times 10^{-14}, 1.26 \times 10^{-14}$	$1.51 \times 10^{-12}, 8.2 \times 10^{-14}$

TABLE XVI. Same Layout as in XI but for $\ell = 4$.

that the extracted ${}_e/{}_o c_1$ values, we find for \mathcal{O}_5 : $|{}_e/{}_o c_1^{n=0}|_{\min, \text{med}, \text{max}} \sim (10^{-21}, 10^{-21}, 10^{-21})$, while for

\mathcal{O}_8 : $|_{o/e}c_1^{n=0}|_{\min, \text{med}, \text{max}} \sim (10^{-24}, 10^{-24}, 10^{-23})$. Thus, for the null operators our $n = 0$ residuals are suppressed well below the levels reported in [1] (quoted there at $\sim 10^{-4}$ in the even sector and $\sim 10^{-6}$ in the odd sector), improving the null-test precision with at least $\sim 15 - 17$ orders of magnitude depending on the solver and parity.

Working with Leaver method, further analysis fitting $\Delta\omega(\zeta)$ with higher-degree polynomials indicates a sizable budget for still-higher powers of ζ due to higher order contamination; accordingly, we interpret the quoted Leaver-based c_1 values as a conservative *upper bound* on any residual $\mathcal{O}(\zeta)$ contamination since unmodeled higher-order terms will leak into lower-order coefficients in finite-window fits.

b. Null Tests: (ii) Ratio between \mathcal{O}_9 and \mathcal{O}_{10} QNM shifts. We also extract QNM shifts sourced by the control operators \mathcal{O}_9 and \mathcal{O}_{10} , which are physical cubic invariants built from the Riemann tensor. On Ricci-flat backgrounds ($R_{\mu\nu} = 0 = R$), we use the identity $\mathcal{O}_9 = 2\mathcal{O}_{10} + \frac{3}{4}\mathcal{O}_5$, so that—up to the (null) \mathcal{O}_5 contamination—setting the Wilson coefficients equal predicts a mode-by-mode ratio $\mathcal{R}_{9/10} = 2$ for the first-order shifts. Computing $\mathcal{R}_{9/10}$ from both EVP and Leaver outputs, we find $\mathcal{R}_{9/10}$ is essentially 2 across the full set of modes, with $\min|\mathcal{R}_{9/10} - 2| \sim 10^{-12}$ and $\max|\mathcal{R}_{9/10} - 2| \lesssim 10^{-9}$ across the full mode set.

Finally, comparing the odd and even sectors for both operators, we confirm that parity isospectrality is broken, with no significant systematic trend.

c. More on Control Operators. We use both EVP and Leaver method to compute fractional frequency shifts δ_{EVP} and δ_{Leaver} for control operators: \mathcal{O}_9 and \mathcal{O}_{10} . Our δ_{EVP} and δ_{Leaver} agrees in magnitude with Ref. [1] when rounded to the two decimal places reported in their Table I.

Moreover, comparing EVP shifts to the linear coefficient $c_1^{(12)}$ extracted from Leaver fits, we find tight mode-by-mode agreement quantified by the symmetric relative difference ϵ_X (computed separately for real ϵ_{\Re} and imaginary ϵ_{\Im} parts). Aggregating all modes and both control operators, we obtain $\min(\epsilon_{\Re}, \epsilon_{\Im}) = (3.54 \times 10^{-17}, 3.54 \times 10^{-16})$, $\text{median}(\epsilon_{\Re}, \epsilon_{\Im}) = (9.48 \times 10^{-14}, 2.66 \times 10^{-14})$, and $\max(\epsilon_{\Re}, \epsilon_{\Im}) = (1.13 \times 10^{-6}, 1.59 \times 10^{-7})$. Almost, the same systematic trends appear here as in the null analysis: disagreement grows with overtone index n and decreases with increasing ℓ . Importantly, the worst-case mismatch occurs precisely where numerical sensitivity is greatest (low ℓ , high n), and is broadly consistent with

the EVP numerical floor inferred from null operators.

d. The main lesson from this work . Viable EFT corrections can lead to *tiny* effects, so modeling them demands end-to-end numerical approaches whose systematic errors are controlled well below the target signal. In this work we provided such a stress test for the MTE/MTF program in HDG. Taken together all the results listed above, we believe MTE has pass stringent null tests in this article, providing a robust foundation for interpreting future beyond-GR ringdown signatures as physical rather than numerical artifacts.

Looking ahead, the same program can be extended in several directions. First, one can move beyond Schwarzschild by developing slow-rotation and ultimately generic Kerr implementations, enabling high-precision cross-checks in HDG parity-violating sectors, and in the presence of additional matter fields (e.g., dCS) [7, 14, 20]. Second, finite- ζ scans can be used to chart the breakdown of linear response and to quantify the onset of higher-order contributions in a controlled manner, complementing EVP's inherently linear sensitivity. In combination with next-generation instruments [2, 4, 6], these extensions will help turn EFT-motivated deformations into robust, model-agnostic strong-field tests using black-hole ringdown.

ACKNOWLEDGMENTS

We acknowledge the partial support of Dr. D.S. through the US National Science Foundation under the Grant No. PHY-2310363. This work was supported by the Natural Sciences and Engineering Research Council (NSERC) of Canada. LL also thanks financial support via the Carlo Fidani Rainer Weiss Chair at Perimeter Institute and CIFAR. Research at Perimeter Institute is supported in part by the Government of Canada through the Department of Innovation, Science and Economic Development and by the Province of Ontario through the Ministry of Colleges and Universities. D. L. acknowledges support from the Simons Foundation (via Award No. 896696), the Simons Foundation International (via Grant No. SFI-MPS-BH-00012593-01), the NSF (via Grants No. PHY-2207650 and PHY-2512423), and the National Aeronautics and Space Administration through award 80NSSC22K0806. P.W. acknowledges funding from the Deutsche Forschungsgemeinschaft (DFG) - project number: 386119226.

[1] C. de Rham, J. Francfort, and J. Zhang, *Phys. Rev. D* **102**, 024079 (2020).
 [2] M. Punturo *et al.*, *Classical and Quantum Gravity* **27**, 194002 (2010).
 [3] M. Maggiore *et al.*, *Journal of Cosmology and Astroparticle Physics* **2020** (03), 050.

[4] D. Reitze *et al.*, *Cosmic explorer: The u.s. contribution to gravitational-wave astronomy beyond ligo* (2019), arXiv:1907.04833 [astro-ph.IM].
 [5] M. Evans *et al.*, *A horizon study for cosmic explorer: Science, observatories, and community* (2021), arXiv:2109.09882 [astro-ph.IM].

- [6] P. Amaro-Seoane *et al.*, *Laser interferometer space antenna* (2017), [arXiv:1702.00786 \[astro-ph.IM\]](#).
- [7] P. A. Cano, K. Fransen, T. Hertog, and S. Maenaut, *Phys. Rev. D* **108**, 124032 (2023).
- [8] E. Berti, V. Cardoso, and A. O. Starinets, *Classical and Quantum Gravity* **26**, 163001 (2009).
- [9] H. O. Silva, G. Tambalo, K. Glampedakis, K. Yagi, and J. Steinhoff, *Phys. Rev. D* **110**, 024042 (2024).
- [10] D. Li, A. Hussain, P. Wagle, Y. Chen, N. Yunes, and A. Zimmerman, *Phys. Rev. D* **109**, 104026 (2024).
- [11] V. Cardoso and L. Gualtieri, *Phys. Rev. D* **80**, 064008 (2009).
- [12] C. Weller, D. Li, and Y. Chen, *Phys. Rev. D* **111**, 024064 (2025).
- [13] D. Li, P. Wagle, Y. Chen, and N. Yunes, *Phys. Rev. X* **13**, 021029 (2023).
- [14] P. Wagle, D. Li, Y. Chen, and N. Yunes, *Phys. Rev. D* **109**, 104029 (2024).
- [15] A. Zimmerman, H. Yang, Z. Mark, Y. Chen, and L. Lehner, in *Gravitational Wave Astrophysics*, edited by C. F. Sopuerta (Springer International Publishing, Cham, 2015) pp. 217–223.
- [16] A. Hussain and A. Zimmerman, *Phys. Rev. D* **106**, 104018 (2022).
- [17] P. Wagle, N. Yunes, and H. O. Silva, *Phys. Rev. D* **105**, 124003 (2022).
- [18] E. W. Leaver, *Proceedings of the Royal Society of London. A. Mathematical and Physical Sciences* **402**, 285 (1985).
- [19] E. W. Leaver, *Phys. Rev. D* **41**, 2986 (1990).
- [20] D. Li, P. Wagle, Y. Chen, and N. Yunes, *Phys. Rev. D* **112**, 044005 (2025).
- [21] J. Lestingi, G. D’Addario, and T. P. Sotiriou, *Phys. Rev. D* **112**, 064070 (2025).
- [22] H. Lü, A. Perkins, C. N. Pope, and K. S. Stelle, *Phys. Rev. Lett.* **114**, 171601 (2015).
- [23] P. A. Cano and A. Ruipérez, *Journal of High Energy Physics* **2019**, 189 (2019).
- [24] S. B. Edgar and A. Höglund, *Journal of Mathematical Physics* **43**, 659 (2002).
- [25] P. A. Cano, K. Fransen, T. Hertog, and S. Maenaut, *Phys. Rev. D* **108**, 024040 (2023).
- [26] S. Chandrasekhar, *The Mathematical Theory of Black Holes* (Clarendon Press, 1983).
- [27] K. Glampedakis, A. D. Johnson, and D. Kennefick, *Phys. Rev. D* **96**, 024036 (2017).
- [28] J. Matyjasek, *Phys. Rev. D* **104**, 084066 (2021).
- [29] M. F. S. Alves, B. P. Pônquio, and L. G. Medeiros, *Phys. Rev. D* **112**, 124007 (2025).
- [30] J. a. G. Rosa and S. R. Dolan, *Phys. Rev. D* **85**, 044043 (2012).
- [31] M. Kaminski, K. Landsteiner, J. Mas, J. P. Shock, and J. Tarrío, *Journal of High Energy Physics* **2010**, 21 (2010).
- [32] V. Cardoso, M. Kimura, A. Maselli, E. Berti, C. F. B. Macedo, and R. McManus, *Phys. Rev. D* **99**, 104077 (2019).
- [33] H.-P. Nollert, *Physical Review D* **47**, 5253 (1993).
- [34] H.-P. Nollert, *Classical and Quantum Gravity* **16**, R159 (1999).
- [35] A. Zhidenko, *Phys. Rev. D* **74**, 064017 (2006).
- [36] R. A. Konoplya and A. Zhidenko, *Rev. Mod. Phys.* **83**, 793 (2011).
- [37] L. C. Stein, *J. Open Source Softw.* **4**, 1683 (2019), [arXiv:1908.10377 \[gr-qc\]](#).
- [38] W. J. Lentz, *Appl. Opt.* **15**, 668 (1976).
- [39] W. H. Press, S. A. Teukolsky, W. T. Vetterling, and B. P. Flannery, *Numerical Recipes: The Art of Scientific Computing*, 3rd ed. (Cambridge University Press, Cambridge, 2007).
- [40] E. Berti, V. Cardoso, and C. M. Will, *Phys. Rev. D* **73**, 064030 (2006).
- [41] H.-P. Nollert, *Classical and Quantum Gravity* **16**, R159 (1999).

Appendix A: Effective potentials

It is convenient to introduce the dimensionless radius

$$y \equiv \frac{r}{r_g}, \quad (\text{A1})$$

and to factor out an overall $1/r_g^2$ from all potentials. We define the coefficients $\alpha_\ell, \beta_\ell, \gamma_\ell, \delta_\ell$ as in the Zerilli sector.

$$\alpha_\ell = \left(\frac{\lambda_\ell}{2} - 1\right)^2 \frac{\lambda_\ell}{2} \quad \beta_\ell = 3/2 \left(\frac{\lambda_\ell}{2} - 1\right)^2 \quad \gamma_\ell = \frac{9}{4} \left(\frac{\lambda_\ell}{2} - 1\right) \quad \delta_\ell = \frac{9}{8} \quad (\text{A2})$$

For the odd/even sectors we have

$$V_{\ell, \text{odd}}^{\text{GR}}(r) = \frac{\lambda_\ell}{r^2} - \frac{3r_g}{r^3} = \frac{1}{r_g^2} \left(\frac{\lambda_\ell}{y^2} - \frac{3}{y^3} \right), \quad V_{\ell, \text{even}}^{\text{GR}}(r) = \frac{8}{r_g^2} \frac{\frac{\delta_\ell}{y^3} + \frac{\gamma_\ell}{y^2} + \frac{\beta_\ell}{y} + \alpha_\ell}{((\lambda_\ell - 2)y + 3)^2}. \quad (\text{A3})$$

a. EFT corrections. We keep d_{58} as the shorthand used in the main text and treat all Wilson coefficients as symbolic.

For the odd-parity sector, the EFT correction (cf. `Vodd` in the code) is

$$V_{\ell,\text{odd}}^{\text{EFT}}(r) = \frac{3}{r_g^2 y^9} \left[d_{58} (24 - 7 \lambda_\ell y) + 6d_9 (80(\lambda_\ell - 6) y^2 + 5(230 - 19\lambda_\ell) y - 662) + \frac{3d_{10}}{2} (160(\lambda_\ell - 6) y^2 + (2300 - 183\lambda_\ell) y - 1348) \right]. \quad (\text{A4})$$

For the even-parity sector, the EFT correction (cf. `Veven` in the code) takes the form

$$V_{\ell,\text{even}}^{\text{EFT}}(r) = -\frac{3}{2r_g^2 y^9 [(\lambda_\ell - 2)y + 3]^3} \left[d_{58} \mathcal{P}_\ell^{(58)}(y) + d_9 \mathcal{P}_\ell^{(9)}(y) + d_{10} \mathcal{P}_\ell^{(10)}(y) \right], \quad (\text{A5})$$

with the polynomials in y given by

$$\mathcal{P}_\ell^{(58)}(y) = 14(\lambda_\ell - 2)^3 \lambda_\ell y^4 + 6(\lambda_\ell - 2)^2 (13\lambda_\ell - 16) y^3 + 270(\lambda_\ell - 2)^2 y^2 + 558(\lambda_\ell - 2) y + 432, \quad (\text{A6})$$

$$\begin{aligned} \mathcal{P}_\ell^{(9)}(y) &= 480(\lambda_\ell - 6)(\lambda_\ell - 2)^3 y^5 - 36(\lambda_\ell - 2)^2 (15\lambda_\ell^2 - 336\lambda_\ell + 836) y^4 - 60(\lambda_\ell - 2)(147\lambda_\ell^2 - 1304\lambda_\ell + 2164) y^3 \\ &\quad - 36(\lambda_\ell - 2)(1073\lambda_\ell - 3988) y^2 - 12(5407\lambda_\ell - 13460) y - 36648, \end{aligned} \quad (\text{A7})$$

$$\begin{aligned} \mathcal{P}_\ell^{(10)}(y) &= 240(\lambda_\ell - 6)(\lambda_\ell - 2)^3 y^5 - 3(\lambda_\ell - 2)^2 (97\lambda_\ell^2 - 2030\lambda_\ell + 5016) y^4 - 3(\lambda_\ell - 2)(1509\lambda_\ell^2 - 13166\lambda_\ell + 21736) y^3 \\ &\quad - 9(\lambda_\ell - 2)(2191\lambda_\ell - 8066) y^2 - 3(11093\lambda_\ell - 27478) y - 18972. \end{aligned} \quad (\text{A8})$$

Appendix B: More Details On Numerical Methods

1. Continued fraction with Nollert-type tail.

We denote by α_n^{GR} , β_n^{GR} , γ_n^{GR} the three-term recurrence coefficients of the GR Schwarzschild problem (either RW or Teukolsky). Introducing the Riccati variable $R_n \equiv a_{n+1}/a_n$, the characteristic equation can be written as [41]

$$\begin{aligned} F(\omega) &\equiv \frac{\beta_0^{GR}}{\alpha_0^{GR}} - R_0(\omega) = 0, \\ R_n(\omega) &= \frac{\gamma_n^{GR}}{\beta_n^{GR} - \alpha_n^{GR} R_{n+1}(\omega)}. \end{aligned} \quad (\text{B1})$$

At large n we assume that the R_n admits an asymptotic expansion of the form

$$R_n(\omega) = R_*(\omega) + b(\omega) n^{-p} + \mathcal{O}(n^{-p-1}), \quad n \rightarrow \infty, \quad (\text{B2})$$

where $R_*(\omega)$ is the large- n limit of $R_n(\omega)$ and $b(\omega)$ is the complex coefficient of the leading n^{-p} correction. In practice we fix a positive exponent p (empirically $p = \frac{1}{2}$ is used), and use this model to construct a Nollert-type tail.

For each trial $\omega_{n\ell}$ we choose a base index N_{tail} (tail start) and two deeper indices $N_1 = N_{\text{tail}} + \Delta N$ and $N_2 = N_{\text{tail}} + 2\Delta N$. Starting from an initial guess for R_{N_1+1} and R_{N_2+1} (we use -1 for both), we propagate backwards using to obtain two approximations $R_{N_{\text{tail}}+1}^{(1)}$ and $R_{N_{\text{tail}}+1}^{(2)}$. Assuming

$$R_{N_k}(\omega) \simeq R_*(\omega) + a(\omega) N_k^{-p}, \quad k = 1, 2, \quad (\text{B3})$$

we solve algebraically for $R_*(\omega)$ and use it as the seed for the backward sweep:

$$R_{N_{\text{tail}}+1}(\omega) \equiv R_*(\omega). \quad (\text{B4})$$

This gives a numerically stable approximation to $R_0(\omega)$, and we then solve the QNM condition $F(\omega) = 0$ using a two-point complex secant method. The precise numerical tolerances and parameter choices for N_{tail} , ΔN , and p are summarized in the III B 1.

2. Series solution, branch tracking, and residuals.

Once ω_0 is fixed, we construct truncated Frobenius series for both the RW and Teukolsky solutions. For RW we use the horizon-based coordinate

$$x_{\text{RW}} = 1 - \frac{r_g}{r}, \quad (\text{B5})$$

and write the master function as

$$\Psi_{\text{RW}}(r) = \mathcal{P}_{\text{RW}}(r, \omega_0) \sum_{n=0}^{N_{\text{max}}} a_n x_{\text{RW}}^n, \quad (\text{B6})$$

where the prefactor \mathcal{P}_{RW} enforces the ingoing horizon and outgoing infinity behaviour,

$$\mathcal{P}_{\text{RW}}(r, \omega_0) = e^{-i\omega_0 \ln(r-r_g) + 2i\omega_0 \ln r + i\omega_0(r-r_g)}. \quad (\text{B7})$$

In the code this prefactor is evaluated using a branch-tracking system that keeps track of the phases of $\ln r$

and $\ln(r - r_g)$ along a chosen path in the complex r -plane. As r is varied, the arguments are adjusted by multiples of 2π so that individual phase jumps are kept below π . A normalization factor \mathcal{N} is fixed at an anchor point $r = r_{\text{anc}} = r_g$ so that the prefactor is continuous and has a fixed phase at that location:

$$\mathcal{P}_{\text{RW}}(r, \omega_0) = \frac{e^{-i\omega_0 \log_{(r-r_g)}(r-r_g) + 2i\omega_0 \log_{(r)}(r) + i\omega_0(r-r_g)}}{\mathcal{N}}, \quad (\text{B8})$$

with \mathcal{N} chosen such that the tracked logarithms coincide with the principal logarithms at $r = r_{\text{anc}}$. This guarantees a consistent asymptotic phase for Ψ_{RW} both along the real axis and along the complex contour. The Teukolsky master function is treated analogously.

Radial derivatives of the series are obtained analytically, and along the contour we also use spectral differentiation in the contour parameter (see below) to compute $dr/d\lambda$ and $dr_*/d\lambda$.

As a sanity check on the series representation, we evaluate the RW and Teukolsky differential operators on a real radial grid $r \in [r_g + \varepsilon, R_{\text{max}}]$, with a small buffer ε above the horizon and a finite outer radius R_{max} . This yields residuals $\mathcal{R}(r)$ for each equation, and we monitor the ∞ -norm

$$\|\mathcal{R}\|_\infty = \max_r |\mathcal{R}(r)|, \quad (\text{B9})$$

for both RW and Teukolsky. In practice, this norm is

many orders of magnitude smaller than unity and is stable under variations of N_{max} and the Nollert tail parameters, confirming that both the tail and the branch-tracked prefactors are correctly capturing the desired boundary conditions.

3. Consistency check in GR.

Before turning on the EFT couplings we perform a stringent self-consistency test of the Leaver+reduction approach. We build a “fat” 12-term Frobenius recurrence for both the RW and Zerilli cases, and then reduce it to a 3-term band by the same high-precision reducer used in the EFT runs. We then solve for the GR frequencies $\omega_{\text{RW}}^{\text{GR}}$ and $\omega_{\text{Z}}^{\text{GR}}$ using the scalar Leaver solver and compare

$$\Delta\omega^{\text{GR}} \equiv \omega_{\text{RW}}^{\text{GR}} - \omega_{\text{Z}}^{\text{GR}}. \quad (\text{B10})$$

Across the tested modes we find $|\Delta\omega^{\text{GR}}| \lesssim 10^{-61}$, comfortably below the continued-fraction truncation error and intrinsic precision floor of the solver. This confirms that the Leaver method and the band-reduction algebra are internally consistent, and that over the entire ζ grid our EFT frequency shifts are measured against GR with an error budget of order 10^{-61} .

TABLE XVII. Power-scaling summary for $\zeta_{\max} = 10^{-4}$ and odd parity. Each p entry is $p_{\text{eff}} \pm \sigma_p$ with the chosen discrete p_* shown as $[p_*]$. C lists the fitted coefficient components $\Re(C) | \Im(C)$ and σ/μ is the flatness ratio.

ℓ	n	\mathcal{O}_9			\mathcal{O}_{10}		
		p	C	σ/μ	p	C	σ/μ
2	0	0.9995 ± 0.0016 [1]	21.14 47.05	2.19×10^{-3}	0.9998 ± 0.0006 [1]	10.53 23.68	8.05×10^{-4}
2	1	1.0000 ± 0.0001 [1]	17.96 70.20	5.36×10^{-3}	0.9999 ± 0.0005 [1]	8.48 35.13	2.24×10^{-3}
2	2	1.0010 ± 0.0031 [1]	-40.36 121.76	2.46×10^{-2}	1.0002 ± 0.0008 [1]	-23.37 58.94	1.07×10^{-2}
2	3	0.9979 ± 0.0133 [1]	-356.62 238.34	3.55×10^{-2}	1.0001 ± 0.0010 [1]	-192.09 103.37	1.34×10^{-2}
3	0	0.9995 ± 0.0018 [1]	18.32 45.78	2.31×10^{-3}	0.9998 ± 0.0006 [1]	9.14 23.06	7.24×10^{-4}
3	1	0.9994 ± 0.0021 [1]	16.01 50.71	3.42×10^{-3}	0.9997 ± 0.0011 [1]	7.87 25.53	1.54×10^{-3}
3	2	1.0000 ± 0.0001 [1]	7.35 61.13	8.11×10^{-3}	0.9998 ± 0.0006 [1]	3.03 30.53	3.28×10^{-3}
3	3	1.0008 ± 0.0023 [1]	-18.09 78.65	2.27×10^{-2}	1.0001 ± 0.0003 [1]	-11.05 38.36	9.56×10^{-3}
4	0	0.9994 ± 0.0018 [1]	17.55 45.23	2.29×10^{-3}	0.9998 ± 0.0005 [1]	8.77 22.78	6.51×10^{-4}
4	1	0.9993 ± 0.0024 [1]	15.94 47.13	3.22×10^{-3}	0.9997 ± 0.0010 [1]	7.91 23.76	1.32×10^{-3}
4	2	0.9993 ± 0.0023 [1]	11.83 51.17	4.81×10^{-3}	0.9996 ± 0.0014 [1]	5.65 25.76	2.14×10^{-3}
4	3	0.9999 ± 0.0005 [1]	3.16 57.89	1.06×10^{-2}	0.9998 ± 0.0008 [1]	0.80 28.89	4.31×10^{-3}

TABLE XVIII. Power-scaling summary for $\zeta_{\max} = 10^{-4}$ and even parity. Each p entry is $p_{\text{eff}} \pm \sigma_p$ with the chosen discrete p_* shown as $[p_*]$. C lists the fitted coefficient components $\Re(C) | \Im(C)$ and σ/μ is the flatness ratio.

ℓ	n	\mathcal{O}_9			\mathcal{O}_{10}		
		p	C	σ/μ	p	C	σ/μ
2	0	1.0000 ± 0.0001 [1]	-12.36 -58.13	8.22×10^{-5}	1.0000 ± 0.0001 [1]	-6.16 -29.07	9.54×10^{-5}
2	1	1.0002 ± 0.0006 [1]	11.00 -55.94	1.12×10^{-3}	1.0000 ± 0.0001 [1]	5.48 -27.88	8.70×10^{-4}
2	2	1.0001 ± 0.0003 [1]	77.00 -53.04	4.74×10^{-3}	0.9999 ± 0.0003 [1]	38.19 -26.71	3.05×10^{-3}
2	3	0.9978 ± 0.0071 [1]	222.39 -55.47	9.22×10^{-3}	0.9986 ± 0.0046 [1]	112.36 -28.89	5.94×10^{-3}
3	0	0.9999 ± 0.0003 [1]	-14.17 -51.72	4.51×10^{-4}	1.0000 ± 0.0001 [1]	-7.07 -25.92	9.08×10^{-5}
3	1	1.0003 ± 0.0010 [1]	-8.04 -53.80	1.17×10^{-3}	1.0001 ± 0.0005 [1]	-3.97 -26.83	6.08×10^{-4}
3	2	1.0004 ± 0.0014 [1]	8.57 -57.45	2.62×10^{-3}	1.0001 ± 0.0003 [1]	4.22 -28.57	1.70×10^{-3}
3	3	1.0004 ± 0.0013 [1]	44.58 -62.00	7.52×10^{-3}	1.0001 ± 0.0002 [1]	21.82 -31.05	4.74×10^{-3}
4	0	0.9998 ± 0.0007 [1]	-14.47 -49.99	8.12×10^{-4}	1.0000 ± 0.0000 [1]	-7.23 -25.08	8.51×10^{-6}
4	1	1.0002 ± 0.0005 [1]	-11.53 -51.47	6.35×10^{-4}	1.0001 ± 0.0004 [1]	-5.72 -25.73	4.84×10^{-4}
4	2	1.0005 ± 0.0017 [1]	-4.25 -54.21	2.06×10^{-3}	1.0002 ± 0.0007 [1]	-2.08 -26.97	1.04×10^{-3}
4	3	1.0006 ± 0.0019 [1]	10.27 -57.84	3.63×10^{-3}	1.0002 ± 0.0005 [1]	5.03 -28.73	2.33×10^{-3}

TABLE XIX. Power-scaling summary for $\zeta_{\max} = 10^{-5}$ and odd parity. Each p entry is $p_{\text{eff}} \pm \sigma_p$ with the chosen discrete p_* shown as $[p_*]$. C lists the fitted coefficient components $\Re(C) | \Im(C)$ and σ/μ is the flatness ratio.

ℓ	n	\mathcal{O}_9			\mathcal{O}_{10}		
		p	C	σ/μ	p	C	σ/μ
2	0	0.9999 ± 0.0002 [1]	21.08 47.48	2.27×10^{-4}	1.0000 ± 0.0001 [1]	10.54 23.76	8.41×10^{-5}
2	1	1.0000 ± 0.0000 [1]	16.52 70.54	5.55×10^{-4}	1.0000 ± 0.0000 [1]	8.21 35.27	2.33×10^{-4}
2	2	1.0001 ± 0.0004 [1]	-50.79 115.86	2.38×10^{-3}	1.0000 ± 0.0001 [1]	-25.66 57.73	1.08×10^{-3}
2	3	1.0002 ± 0.0007 [1]	-392.50 188.29	2.64×10^{-3}	1.0001 ± 0.0003 [1]	-196.30 92.89	1.22×10^{-3}
3	0	0.9999 ± 0.0002 [1]	18.29 46.22	2.41×10^{-4}	1.0000 ± 0.0001 [1]	9.14 23.13	7.58×10^{-5}
3	1	0.9999 ± 0.0002 [1]	15.68 51.32	3.54×10^{-4}	1.0000 ± 0.0001 [1]	7.83 25.68	1.61×10^{-4}
3	2	1.0000 ± 0.0000 [1]	5.46 61.30	8.43×10^{-4}	1.0000 ± 0.0001 [1]	2.67 30.64	3.42×10^{-4}
3	3	1.0001 ± 0.0003 [1]	-24.49 75.96	2.27×10^{-3}	1.0000 ± 0.0000 [1]	-12.42 37.87	9.79×10^{-4}
4	0	0.9999 ± 0.0002 [1]	17.55 45.66	2.41×10^{-4}	1.0000 ± 0.0001 [1]	8.77 22.85	6.81×10^{-5}
4	1	0.9999 ± 0.0002 [1]	15.82 47.73	3.36×10^{-4}	1.0000 ± 0.0001 [1]	7.90 23.88	1.39×10^{-4}
4	2	0.9999 ± 0.0002 [1]	11.15 51.86	4.97×10^{-4}	1.0000 ± 0.0001 [1]	5.55 25.94	2.23×10^{-4}
4	3	1.0000 ± 0.0000 [1]	0.82 58.02	1.11×10^{-3}	1.0000 ± 0.0001 [1]	0.33 29.00	4.49×10^{-4}

TABLE XX. Power-scaling summary for $\zeta_{\max} = 10^{-5}$ and even parity. Each p entry is $p_{\text{eff}} \pm \sigma_p$ with the chosen discrete p_* shown as $[p_*]$. C lists the fitted coefficient components $\Re(C) | \Im(C)$ and σ/μ is the flatness ratio.

ℓ	n	\mathcal{O}_9			\mathcal{O}_{10}		
		p	C	σ/μ	p	C	σ/μ
2	0	1.0000 ± 0.0000 [1]	-12.34 -58.12	8.48×10^{-6}	1.0000 ± 0.0000 [1]	-6.17 -29.06	9.97×10^{-6}
2	1	1.0000 ± 0.0001 [1]	10.78 -55.83	1.18×10^{-4}	1.0000 ± 0.0000 [1]	5.39 -27.90	9.09×10^{-5}
2	2	1.0000 ± 0.0000 [1]	75.93 -54.33	5.14×10^{-4}	1.0000 ± 0.0000 [1]	37.93 -27.19	3.24×10^{-4}
2	3	0.9998 ± 0.0007 [1]	228.70 -60.79	9.85×10^{-4}	0.9998 ± 0.0005 [1]	114.46 -30.53	6.27×10^{-4}
3	0	1.0000 ± 0.0000 [1]	-14.15 -51.81	4.69×10^{-5}	1.0000 ± 0.0000 [1]	-7.07 -25.91	9.37×10^{-6}
3	1	1.0000 ± 0.0001 [1]	-8.00 -53.56	1.21×10^{-4}	1.0000 ± 0.0000 [1]	-3.99 -26.77	6.34×10^{-5}
3	2	1.0001 ± 0.0002 [1]	8.09 -57.13	2.75×10^{-4}	1.0000 ± 0.0000 [1]	4.04 -28.55	1.77×10^{-4}
3	3	1.0001 ± 0.0002 [1]	42.58 -62.80	8.05×10^{-4}	1.0000 ± 0.0000 [1]	21.24 -31.40	5.03×10^{-4}
4	0	1.0000 ± 0.0001 [1]	-14.46 -50.15	8.40×10^{-5}	1.0000 ± 0.0000 [1]	-7.23 -25.08	8.95×10^{-7}
4	1	1.0000 ± 0.0001 [1]	-11.45 -51.36	6.50×10^{-5}	1.0000 ± 0.0000 [1]	-5.72 -25.68	5.02×10^{-5}
4	2	1.0001 ± 0.0002 [1]	-4.28 -53.79	2.14×10^{-4}	1.0000 ± 0.0001 [1]	-2.13 -26.88	1.09×10^{-4}
4	3	1.0001 ± 0.0002 [1]	9.57 -57.44	3.79×10^{-4}	1.0000 ± 0.0001 [1]	4.77 -28.70	2.43×10^{-4}

TABLE XXI. Power-scaling summary for $\zeta_{\max} = 10^{-4}$ and odd parity. Each p entry is $p_{\text{eff}} \pm \sigma_p$ with the chosen discrete p_* shown as $[p_*]$. C lists the fitted coefficient components $\Re(C) | \Im(C)$ and σ/μ is the flatness ratio.

ℓ	n	\mathcal{O}_5			\mathcal{O}_8		
		p	C	σ/μ	p	C	σ/μ
2	0	2.0001 ± 0.0004 [2]	120.58 478.06	5.24×10^{-4}	2.0000 ± 0.0001 [2]	7.50 29.83	1.31×10^{-4}
2	1	2.0003 ± 0.0011 [2]	-34.19 599.67	1.42×10^{-3}	2.0001 ± 0.0003 [2]	-2.21 37.31	3.54×10^{-4}
2	2	2.0004 ± 0.0013 [2]	-688.49 745.87	1.91×10^{-3}	2.0001 ± 0.0003 [2]	-42.97 46.20	4.73×10^{-4}
2	3	2.0006 ± 0.0020 [2]	-2824.48 939.68	2.44×10^{-3}	2.0002 ± 0.0005 [2]	-175.20 57.87	6.05×10^{-4}
3	0	2.0000 ± 0.0001 [2]	157.29 482.03	3.60×10^{-4}	2.0000 ± 0.0000 [2]	9.80 30.15	8.93×10^{-5}
3	1	2.0001 ± 0.0005 [2]	138.01 599.74	7.75×10^{-4}	2.0000 ± 0.0001 [2]	8.54 37.43	1.94×10^{-4}
3	2	2.0004 ± 0.0012 [2]	30.54 762.00	1.82×10^{-3}	2.0001 ± 0.0003 [2]	1.70 47.40	4.52×10^{-4}
3	3	2.0005 ± 0.0016 [2]	-325.04 990.95	2.82×10^{-3}	2.0001 ± 0.0004 [2]	-20.64 61.38	6.98×10^{-4}
4	0	1.9999 ± 0.0004 [2]	166.35 462.13	6.16×10^{-4}	2.0000 ± 0.0001 [2]	10.37 28.95	1.53×10^{-4}
4	1	2.0000 ± 0.0000 [2]	170.06 556.24	5.21×10^{-4}	2.0000 ± 0.0000 [2]	10.56 34.78	1.30×10^{-4}
4	2	2.0002 ± 0.0005 [2]	155.13 679.07	1.12×10^{-3}	2.0000 ± 0.0001 [2]	9.54 42.38	2.80×10^{-4}
4	3	2.0004 ± 0.0012 [2]	74.34 855.61	2.17×10^{-3}	2.0001 ± 0.0003 [2]	4.32 53.23	5.39×10^{-4}

TABLE XXII. Power-scaling summary for $\zeta_{\max} = 10^{-4}$ and even parity. Each p entry is $p_{\text{eff}} \pm \sigma_p$ with the chosen discrete p_* shown as $[p_*]$. C lists the fitted coefficient components $\Re(C) | \Im(C)$ and σ/μ is the flatness ratio.

ℓ	n	\mathcal{O}_5			\mathcal{O}_8		
		p	C	σ/μ	p	C	σ/μ
2	0	2.0001 ± 0.0004 [2]	125.28 498.26	5.29×10^{-4}	2.0000 ± 0.0001 [2]	7.79 31.09	1.32×10^{-4}
2	1	2.0003 ± 0.0011 [2]	-41.76 602.93	1.48×10^{-3}	2.0001 ± 0.0003 [2]	-2.68 37.50	3.68×10^{-4}
2	2	2.0004 ± 0.0014 [2]	-713.18 721.64	1.92×10^{-3}	2.0001 ± 0.0003 [2]	-44.47 44.69	4.76×10^{-4}
2	3	2.0006 ± 0.0021 [2]	-2812.74 849.70	2.49×10^{-3}	2.0002 ± 0.0005 [2]	-174.38 52.35	6.19×10^{-4}
3	0	2.0000 ± 0.0001 [2]	158.94 488.04	3.68×10^{-4}	2.0000 ± 0.0000 [2]	9.90 30.53	9.11×10^{-5}
3	1	2.0001 ± 0.0005 [2]	138.16 604.53	7.89×10^{-4}	2.0000 ± 0.0001 [2]	8.54 37.73	1.97×10^{-4}
3	2	2.0004 ± 0.0012 [2]	25.61 764.80	1.83×10^{-3}	2.0001 ± 0.0003 [2]	1.40 47.57	4.57×10^{-4}
3	3	2.0005 ± 0.0016 [2]	-342.02 985.70	2.78×10^{-3}	2.0001 ± 0.0004 [2]	-21.68 61.05	6.90×10^{-4}
4	0	1.9999 ± 0.0004 [2]	167.00 464.14	6.23×10^{-4}	2.0000 ± 0.0001 [2]	10.41 29.07	1.55×10^{-4}
4	1	2.0000 ± 0.0000 [2]	170.55 558.24	5.23×10^{-4}	2.0000 ± 0.0000 [2]	10.59 34.91	1.30×10^{-4}
4	2	2.0002 ± 0.0006 [2]	154.75 681.43	1.13×10^{-3}	2.0000 ± 0.0001 [2]	9.51 42.52	2.82×10^{-4}
4	3	2.0004 ± 0.0012 [2]	71.22 857.42	2.17×10^{-3}	2.0001 ± 0.0003 [2]	4.12 53.34	5.41×10^{-4}

TABLE XXIII. Power-scaling summary for $\zeta_{\max} = 10^{-5}$ and odd parity. Each p entry is $p_{\text{eff}} \pm \sigma_p$ with the chosen discrete p_* shown as $[p_*]$. C lists the fitted coefficient components $\Re(C) | \Im(C)$ and σ/μ is the flatness ratio.

ℓ	n	\mathcal{O}_5			\mathcal{O}_8		
		p	C	σ/μ	p	C	σ/μ
2	0	2.0000 ± 0.0000 [2]	119.93 477.18	5.48×10^{-5}	2.0000 ± 0.0000 [2]	7.49 29.82	1.37×10^{-5}
2	1	2.0000 ± 0.0001 [2]	-35.58 596.37	1.47×10^{-4}	2.0000 ± 0.0000 [2]	-2.23 37.26	3.68×10^{-5}
2	2	2.0000 ± 0.0001 [2]	-687.38 737.82	1.97×10^{-4}	2.0000 ± 0.0000 [2]	-42.96 46.07	4.93×10^{-5}
2	3	2.0001 ± 0.0002 [2]	-2798.98 923.16	2.52×10^{-4}	2.0000 ± 0.0001 [2]	-174.80 57.61	6.30×10^{-5}
3	0	2.0000 ± 0.0000 [2]	156.71 482.55	3.72×10^{-5}	2.0000 ± 0.0000 [2]	9.79 30.16	9.28×10^{-6}
3	1	2.0000 ± 0.0000 [2]	136.30 598.69	8.08×10^{-5}	2.0000 ± 0.0000 [2]	8.51 37.41	2.02×10^{-5}
3	2	2.0000 ± 0.0001 [2]	26.59 757.72	1.88×10^{-4}	2.0000 ± 0.0000 [2]	1.64 47.34	4.71×10^{-5}
3	3	2.0001 ± 0.0002 [2]	-331.30 980.32	2.91×10^{-4}	2.0000 ± 0.0000 [2]	-20.74 61.21	7.26×10^{-5}
4	0	2.0000 ± 0.0000 [2]	165.88 463.33	6.36×10^{-5}	2.0000 ± 0.0000 [2]	10.36 28.96	1.59×10^{-5}
4	1	2.0000 ± 0.0000 [2]	168.83 556.57	5.40×10^{-5}	2.0000 ± 0.0000 [2]	10.55 34.79	1.35×10^{-5}
4	2	2.0000 ± 0.0001 [2]	152.10 677.80	1.17×10^{-4}	2.0000 ± 0.0000 [2]	9.49 42.36	2.92×10^{-5}
4	3	2.0000 ± 0.0001 [2]	68.03 850.98	2.25×10^{-4}	2.0000 ± 0.0000 [2]	4.22 53.16	5.62×10^{-5}

TABLE XXIV. Power-scaling summary for $\zeta_{\max} = 10^{-5}$ and even parity. Each p entry is $p_{\text{eff}} \pm \sigma_p$ with the chosen discrete p_* shown as $[p_*]$. C lists the fitted coefficient components $\Re(C) | \Im(C)$ and σ/μ is the flatness ratio.

ℓ	n	\mathcal{O}_5			\mathcal{O}_8		
		p	C	σ/μ	p	C	σ/μ
2	0	2.0000 ± 0.0000 [2]	124.59 497.35	5.52×10^{-5}	2.0000 ± 0.0000 [2]	7.78 31.08	1.38×10^{-5}
2	1	2.0000 ± 0.0001 [2]	-43.13 599.43	1.54×10^{-4}	2.0000 ± 0.0000 [2]	-2.70 37.45	3.84×10^{-5}
2	2	2.0000 ± 0.0001 [2]	-711.25 713.70	1.98×10^{-4}	2.0000 ± 0.0000 [2]	-44.44 44.57	4.96×10^{-5}
2	3	2.0001 ± 0.0002 [2]	-2785.66 835.26	2.58×10^{-4}	2.0000 ± 0.0001 [2]	-173.96 52.13	6.44×10^{-5}
3	0	2.0000 ± 0.0000 [2]	158.35 488.58	3.79×10^{-5}	2.0000 ± 0.0000 [2]	9.89 30.54	9.47×10^{-6}
3	1	2.0000 ± 0.0000 [2]	136.42 603.43	8.23×10^{-5}	2.0000 ± 0.0000 [2]	8.52 37.71	2.06×10^{-5}
3	2	2.0000 ± 0.0001 [2]	21.70 760.38	1.90×10^{-4}	2.0000 ± 0.0000 [2]	1.34 47.50	4.76×10^{-5}
3	3	2.0001 ± 0.0002 [2]	-347.86 974.99	2.87×10^{-4}	2.0000 ± 0.0000 [2]	-21.77 60.88	7.17×10^{-5}
4	0	2.0000 ± 0.0000 [2]	166.53 465.36	6.44×10^{-5}	2.0000 ± 0.0000 [2]	10.41 29.09	1.61×10^{-5}
4	1	2.0000 ± 0.0000 [2]	169.30 558.58	5.43×10^{-5}	2.0000 ± 0.0000 [2]	10.57 34.91	1.36×10^{-5}
4	2	2.0000 ± 0.0001 [2]	151.70 680.12	1.18×10^{-4}	2.0000 ± 0.0000 [2]	9.47 42.50	2.94×10^{-5}
4	3	2.0000 ± 0.0001 [2]	64.93 852.71	2.25×10^{-4}	2.0000 ± 0.0000 [2]	4.03 53.27	5.63×10^{-5}